The complex jet- and bar-perturbed kinematics in NGC 3393 as revealed with ALMA and GEMINI–GMOS/IFU

Carolina Finlez,[1]★ Neil M. Nagar,[1] Thaisa Storchi-Bergmann,[2] Allan Schnorr-Müller,[2] Rogemar A. Riffel,[3] Davide Lena,[4,5] C. G. Mundell[6] and Martin S. Elvis[7]

[1]*Departamento de Astronomía, Universidad de Concepción, Casilla 160-C, Concepción, Chile*
[2]*Instituto de Física, Universidade Federal do Rio Grande do Sul, 91501-970 Porto Alegre, RS, Brazil*
[3]*Departamento de Física, Centro de Ciencias Naturales e Exatas, Universidade Federal de Santa Maria, 97105-900 Santa Maria, RS, Brazil*
[4]*SRON Netherlands Institute for Space Research, Sorbonnelaan 2, NL-3584 CA Utretch, the Netherlands*
[5]*Department of Astrophysics/IMAPP, Radboud University, Nijmegen, PO Box 9010, NL-6500 GL Nijmegen, the Netherlands*
[6]*Department of Physics, University of Bath, Claverton Down, Bath BA2 7AY, UK*
[7]*Harvard-Smithsonian Center for Astrophysics, 60 Garden St., Cambridge, MA 02138, USA*

ABSTRACT

NGC 3393, a nearby Seyfert 2 galaxy with nuclear radio jets, large-scale and nuclear bars, and a posited secondary supermassive black hole, provides an interesting laboratory to test the physics of inflows and outflows. Here we present and analyse the molecular gas [ALMA observations of CO J:2-1 emission over a field of view (FOV) of 45 arcsec × 45 arcsec, at $0\overset{''}{.}56$ (143 pc) spatial and $5 \,\mathrm{km\,s^{-1}}$ spectral resolution), ionized gas and stars (GEMINI–GMOS/IFU; over an FOV of 4 arcsec × 5 arcsec, at $0\overset{''}{.}62$ (159 pc) spatial and $23 \,\mathrm{km\,s^{-1}}$ spectral resolution) in NGC 3393. The ionized gas emission, detected over the complete GEMINI–GMOS FOV, has three identifiable kinematic components. A narrow ($\sigma < 115 \,\mathrm{km\,s^{-1}}$) component present in the complete FOV, which is consistent with rotation in the galaxy disc. A broad ($\sigma > 115 \,\mathrm{km\,s^{-1}}$) redshifted component, detected near the NE and SW radio lobes; which we interpret as a radio jet-driven outflow. And a broad ($\sigma > 115 \,\mathrm{km\,s^{-1}}$) blueshifted component that shows high velocities in a region perpendicular to the radio jet axis; we interpret this as an equatorial outflow. The CO J:2-1 emission is detected in spiral arms on 5–20 arcsec scales, and in two disturbed circumnuclear regions. The molecular kinematics in the spiral arms can be explained by rotation. The highly disturbed kinematics of the inner region can be explained by perturbations induced by the nuclear bar and interactions with the large scale bar. We find no evidence for, but cannot strongly rule out, the presence of the posited secondary black hole.

Key words: black hole physics – galaxies: active – galaxies: individual: (NGC 3393) – galaxies: kinematics and dynamics – galaxies: nuclei – galaxies: Seyfert.

1 INTRODUCTION

It is widely accepted that most – if not all – nearby galaxies with a bulge component host a supermassive black hole (SMBH) in their centre (e.g. Kormendy & Richstone 1995; Ferrarese & Merritt 2000; Ferrarese & Ford 2005). A considerable amount of observational evidence supports a connection between SMBH and the host galaxy growth, the main one being a strong correlation between the mass of the SMBH and the properties of the bulge of the host galaxy (Gebhardt et al. 2000). Nevertheless, the details of coevolution of the SMBH and the host galaxy remain the subject of an ongoing debate.

Despite the ubiquity of SMBHs at the centre of galaxies, only a small fraction of these are active galactic nuclei (AGN) in the local universe (e.g. Ho, Filippenko & Sargent 1997; Kewley et al. 2006). The questions of what triggers activity in a galactic centre and if this ignition mechanism is related to the host galaxy properties, arise naturally. The lack of activity in the nucleus can be related to a lack of accretion material or the absence of a fuelling mechanism. The amount of gas needed to fuel an AGN over a normal duty cycle is a large fraction of the total gas contained in the galaxy (Combes 2001), thus a fuelling mechanism must be able to remove most of the angular momentum of a large amount of gas so this can be transferred from the kpc-scale into the sub-pc central region to feed the AGN.

Gravitational mechanisms such as galaxy interactions can drive gas inwards. Major mergers are thought to be responsible for the

★ E-mail: cfinlez@udec.cl

high accretion rate observed in luminous quasars, while minor mergers can produce Seyfert-level luminosities. Alternatively, secular mechanisms can also remove angular momentum and drive gas towards the nucleus. Observations point to secular processes being the most common triggering mechanisms for medium-to-low luminosity AGNs (e.g. Treister et al. 2012; Hopkins, Kocevski & Bundy 2014; Fan et al. 2016; Goulding et al. 2018).

Non-axisymmetric potentials, such as spiral structures and bars can produce radial inflows to the central region, which can be observed as line-of-sight velocity distortions (Lin & Shu 1964; Lindblad 1964). Gas transport via bars is efficient (e.g. Mundell & Shone 1999) from large scale down to the inner kpc, where gas can get stalled in rings at the inner Lindblad resonance region (Combes & Gerin 1985). From this scale to the centre, other mechanisms can be invoked to transport gas to the AGN, such as inner spiral structures and bars within bars (Shlosman, Frank & Begelman 1989).

The incidence of bars is similar in both active and non-active galaxies and thus a strong correlation between bar presence and activity is yet to be found (e.g. Knapen, Shlosman & Peletier 2000; Cisternas et al. 2013; Cheung et al. 2015; Galloway et al. 2015; Goulding et al. 2017). However a difference between active and inactive galaxies has been observed by Simões Lopes et al. (2007) and Martini & Pogge (1999). Using a sample of active and control galaxy pairs, they observed nuclear dust spirals and structures in 100 per cent of the active early-type galaxies, but in only 25 per cent of the control sample. This dust excess has been confirmed by Martini, Dicken & Storchi-Bergmann (2013), and is thought to trace the feeding channels to the AGN (Ferrarese & Ford 2005; Storchi-Bergmann et al. 2007; Kormendy & Ho 2013). Similarly, in a study of ionized gas dynamics in a matched sample of active and inactive galaxies, Dumas et al. (2007), identified increased kinematics disturbance as a function of accretion rate in the inner 1 kpc of an AGN, where activity and dynamical time-scales become comparable.

The non-axisymmetric gravitational potential created by a bar can produce important kinematic effects on the gas which have been studied by hydrodynamical (e.g. Athanassoula 1992; Lindblad, Lindblad & Athanassoula 1996; Kim et al. 2012) and/or *N*-body simulations (e.g. Sellwood 1981; Emsellem et al. 2001a). A different method to gain insight on these kinematic effects is to quantify the line-of-sight deviations from pure rotation, which can be achieved from linear perturbation theory (Lin & Shu 1964). The non-axisymmetric distortions to the planar flow can be decomposed in their harmonic components. Franx, van Gorkom & de Zeeuw (1994) and Schoenmakers, Franx & de Zeeuw (1997a) pioneered an approach to interpret these harmonic coefficients based on epicycle theory, and thus only valid for small departures from circular orbit speed. Since then, this harmonic decomposition analysis has been carried by several authors (e.g. Emsellem et al. 2001b; Wong, Blitz & Bosma 2004).

One aspect of the SMBH–host galaxy connection is the interaction between the gas of the host galaxy and the energy generated by the AGN, which produces a feedback process that has been theorized as an important component in galaxy evolution as it can help to regulate the growth of the galaxy, preventing it from becoming too massive (Di Matteo, Springel & Hernquist 2005; Wagner & Bicknell 2011; Fabian 2012).

This interaction can occur, broadly, in two main modes: radiative or quasar mode and kinetic or radio mode (Croton et al. 2006; Fabian 2012). The former is driven by a wind caused by the accretion of material into the SMBH, producing wide-angle sub-relativistic outflows. The latter is driven by relativistic radio jets. Both these winds and jets can have important consequences in the galaxy evolution as they can heat and ionize cold gas when colliding with it, preventing the gas from collapsing under self-gravity, thus halting the accretion onto the SMBH and quenching star formation (e.g. Best et al. 2005; Hardcastle et al. 2013). The jets can also directly expel gas from the galaxy removing the components for further star formation (Nesvadba et al. 2006). However, some simulations (e.g. Antonuccio-Delogu & Silk 2010; Silk & Nusser 2010) reveal that jet activity is able to trigger star formation by producing high-density cavities with low temperature, which are embedded in a cocoon around the jet (e.g. Best et al. 1998; Jarvis et al. 2001), a scenario known as positive radio mode feedback. The alignment of the outflowing gas with the jet suggests that the outflows are driven by the transfer of energy and momentum from the radio jet to the interstellar medium (ISM), as shown by hydrodynamical simulations (Wagner, Bicknell & Umemura 2012). Jet-driven outflows have been observed in neutral and molecular gas (e.g. Morganti et al. 2005; Dasyra & Combes 2012) and in the ionized gas (e.g. Riffel et al. 2006; Holt et al. 2011; Couto, Storchi-Bergmann & Schnorr-Müller 2017). Kinematic features consistent with gas inflows and outflows have been found in the ionized and molecular gas of the central region of nearby galaxies (e.g. García-Burillo et al. 2005; Lena et al. 2016; Schnorr-Müller et al. 2016, 2017, and references therein).

In this work we analyse the bar- and jet-induced perturbations on the molecular and ionized gas in NGC 3393 using new data from ALMA (CO J:2-1) and data obtained with the Integral Field Unit of the Gemini Multi Object Spectrograph at the Gemini South telescope (hereafter refered to as GEMINI-GMOS/IFU), this data consists of optical spectra with information from stars and gas. NGC 3393 is a nearby, bright ($m_b = 13.1$ according to de Vaucouleurs et al. 1991), spiral (Sa) galaxy, at an estimated redshift of 0.012442 (optical), or 0.012509 (from the 21 cm line) which corresponds to a luminosity distance of 52 Mpc and a scale of 0.25 kpc arcsec^{-1}, assuming $H_o = 73$ km s^{-1} Mpc^{-1}. The galaxy covers over 1 arcmin on the sky, it is observed nearly face-on, and it has been classified optically as a Seyfert 2 (Véron-Cetty & Véron 2003). It is interacting weakly with a nearby companion that is 60 kpc away (Schmitt et al. 2001).

From neutral hydrogen (HI) single dish observations the maximum rotation velocity corrected by inclination is 158 ± 7 km s^{-1}, and the central velocity dispersion is 197 ± 28 km s^{-1} (Paturel et al. 2003). Near Infrared (NIR) images show a stellar bar in position angle (PA) $\sim 159°-165°$, with maximum ellipticity $e_{max} = 0.2$, and semimajor axis (SMA) 13 arcsec. A faint nuclear bar has also been posited in PA $\sim 145°-150°$, $e_{max} = 0.46$, and SMA 2 arcsec (Jungwiert, Combes & Axon 1997; Alonso-Herrero et al. 1998). Läsker et al. (2016) modelled the light distribution of the galaxy using *HST* imaging and found two prominent rings: the first is actually a partial ring formed by two asymmetric tightly-wound spiral arms in an outer disc of radius 40 arcsec; the second is an inner ring that appears elongated, with a radius of 13 arcsec, i.e. coincident with the outer bar identified by Alonso-Herrero et al. (1998). These authors derive a PA of 140° for the 2 arcsec SMA inner bar.

A high resolution *HST* [O III] emission line image of the narrow-line region (NLR; Schmitt et al. 2003) shows an S-shaped morphology with arms that show an opening angle of 90°, and an extension of 5.6 arcsec pc (1410 pc along the ionization axis PA) × 3 arcsec (740 pc), with the ionization axis oriented in PA 65°. Their derived PA is only slightly different from the value of 55° quoted by Schmitt & Kinney (1996) and Cooke et al. (2000). The sense of curvature of this S-shape is the same as the large-scale spiral arms. The [O III]

emission extends up to $r \sim 15$ arcsec (3750 pc) along PA 44°. This S-shaped structure of high-excitation gas surrounds a three-component radio structure, as observed with the very large array (VLA) at 1.5, 4 and 8.4 GHz (Cooke et al. 2000; Koss et al. 2015). The central radio source is unresolved and has a flatter spectrum than the lobes. Chandra data were also obtained by Bianchi, Guainazzi & Chiaberge (2006) and Levenson et al. (2006), who found soft X-ray emission that has strong morphological correlations with the extended [O III] emission.

The kinematics of the NLR has been studied by Cooke et al. (2000) using Fabry-Pérot [N II] data. They found a skew between the velocity fields of the inner region and that of the outer arms, and fitted a rotation curve that indicates that the major axis of the galaxy goes from NE to SW along PA 68°, with the NE gas receding and the SW gas approaching. Assuming trailing arms, Cooke et al. (2000) concludes that the galaxy is rotating counterclockwise.

Using Chandra X-ray observations, Fabbiano et al. (2011) reported the presence of two X-ray sources which they suggested were obscured AGNs, separated by ∼130 pc, with lower mass limits of $\sim 8 \times 10^5$ M$_\odot$ for the NE source and $\sim 10^6$ M$_\odot$ for the SW source. More recent observations and analysis by Koss et al. (2015) found the same morphological correlations between the [O III], X-ray, and radio emission, but they conclude that the double SMBH detection is most likely spurious, resulting from the low number of X-ray counts (<160) at 6–7 keV and data smoothing with a few counts per pixel on scales much smaller than the point spread function.

NGC 3393 is a Compton thick galaxy (Koss et al. 2015) and has polarized broad $H\alpha$ and $H\beta$ emission lines (Kay, Tran & Magalhães 2002; Ramos Almeida et al. 2016). A water maser emitting disc has been observed in the nuclear region using very long baseline interferometry observations (Kondratko, Greenhill & Moran 2008): this water maser disc is observed edge on, with a major axis in PA $\sim -34°$, i.e. perpendicular to the NLR axis. The kinematics of the water masers in the disc are consistent with Keplerian rotation, with an enclosed mass of $(3.1 \pm 0.2) \times 10^7$ M$_\odot$.

This paper is organized as follows. In Section 2 we describe the observations and data reductions. In Section 3 we present the methods used for the analysis and the subsequent results. In Section 4 we present a discussion of the results and in Section 5 we present our conclusions.

2 OBSERVATIONS AND DATA REDUCTION

2.1 GEMINI–GMOS/IFU

The observations were obtained with the Integral Field Unit of the Gemini Multi Object Spectrograph (GMOS/IFU; Allington-Smith et al. 2002; Hook et al. 2004) at the Gemini South Telescope on 2015 June 20 (project GS-2015A-Q-12). The observations were made in 'single-slit' mode, using the IFU-R mask, and the B600+G5323 grating with four exposures of 720 s each, adding small spatial (0″.5) and spectral (50 Å) offsets for every exposure. The spectral coverage of the observations was 4092−7336 Å, at a spectral resolution of $R = 1688$, covering the emission lines $H\beta$, [O III] λλ4959, 5007, [O I] λ6300, $H\alpha$, [N II] λλ6548, 6583, and [S II] λλ6717, 6731, in addition to several stellar absorption lines. The standard star used for flux calibration is LTT 7987, which was observed on 2015 May 30. The field of view (FOV) of the observations was 3″.8 × 4″.9, which corresponds to a size of 0.96 kpc × 1.24 kpc in the galaxy, sampled at 0″.08.

Seeing during the observations was 0″.62 as measured from the full width at half-maximum of the spatial profile of the stars in the acquisition image; at the galaxy this corresponds to 155 pc.

The data processing was performed using tasks from the GEMINI.GMOS package for IRAF, following Lena (2014). This process includes bias subtraction, flat fielding, sky subtraction, wavelength calibration, flux calibration, differential atmospheric dispersion, and finally, the building of the data cubes with a sampling of 0″.2 × 0″.2. The four individual data cubes are combined to avoid the detector gaps, obtaining the final data cube used throughout this paper.

The GMOS continuum image, made by collapsing channels of the data cube that did not include strong emission lines, the FOV orientation and example spectra are shown in Fig. 1.

2.2 ALMA: CO J:2-1

NGC 3393 was observed on 2016 May 3 as part of Project 2015.1.00086.S (P.I. Nagar). Four basebands (spw's) were used: each set to an effective bandwidth of 1.875 GHz. Spw1 was centred on the CO J:2-1 line ($\nu_{rest} = 230.538$ GHz), with a channel width of 2.5 km s^{-1}. Spw2 was set to 'TDM' mode, for highest sensitivity, and used to cover the continuum centred on $\nu_{rest} = 232.538$ GHz with 40.8 km s^{-1} channels. Spw3 was centred on the CS J:5-4 line ($\nu_{rest} = 244.935$ GHz), with a channel width of 5.1 km s^{-1}. Spw4 was set to 'TDM' mode, for highest sensitivity, and used to cover the continuum centred on $\nu_{rest} = 246.936$ GHz with 31.3 km s^{-1} channels. 41 antennas were used and the total integration time on NGC 3393 was ∼26 min. 6 min scans on NGC 3393 were interleaved with 1 min scans on the nearby 'phase-calibrator' J1037-2934. The latter is a well-studied compact quasar at redshift 0.312 with a position accurate to better than 1 mas. No flux calibrator was observed within this 'scheduling block'.

Data were calibrated and imaged using CASAversion 4.7, and mostly followed the calibration script provided by the ALMA observatory (the CASA calibration pipeline was not available at the time of the release of this dataset). Since a flux calibrator was not observed for this project, flux calibration was performed by setting the flux of the phase calibrator J1037-2934 to 602 mJy at 235.7 GHz (a value provided in the ALMA observatories calibration script). The ALMA calibrator data base shows that this source had a measured flux of 630 mJy when observed 12 days later at the same frequency. The continuum was imaged from line-free channels in all four spws. This continuum image, at an effective frequency of 239 GHz, was made using 'Briggs weighting' with robust = 2, i.e. 'natural' weighting. The synthesized beam of this image has a major (minor) axis of 0″.71 (0″.61) in PA 85° and the rms noise is 0.023 mJy beam^{-1}. The continuum-subtracted uv-data were then used to image the CO J:2-1 line. The final CO J:2-1 data we use and show in this work come from two data cubes: (i) a higher spatial and spectral resolution cube, made using 'Briggs weighting' with robust = 0.2, and using the intrinsic spectral resolution. This data cube has a synthesized beam with major (minor axis) of 0″.58 (0″.5) with a beam PA of −72° and an rms noise of 0.7 mJy beam^{-1} per 2.5 km s^{-1} channel; (ii) a lower spatial and spectral resolution (but higher signal to noise) cube, made using 'natural' weighting, and a four-channel spectral averaging. This data cube has a synthesized beam with major (minor) axis of 0″.73 (0″.62) with a beam PA of 86° and an rms noise of 0.45 mJy beam^{-1} per 10 km s^{-1} channel.

The ALMA integrated intensity map is shown as black contours in Fig. 2, to show the relative orientation with the GEMINI-GMOS/IFU FOV and help the reader better understand the maps shown in this paper.
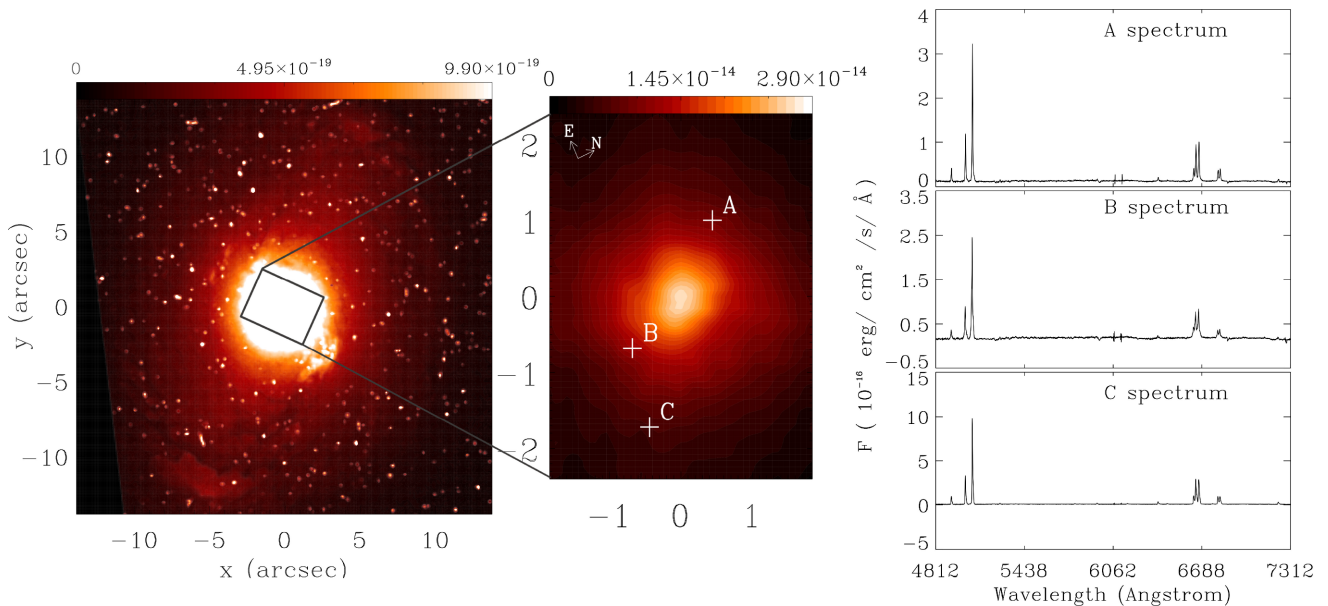
Figure 1. Left: *HST* F606W image for the galaxy, overlaid with the GMOS FOV. Orientation is N to the top and E to the left; Middle: GMOS continuum image, made by collapsing channels of the data cube that did not include strong emission lines. Orientation is shown with the compass in the top left corner; Right: Example spectra for the three points marked on the continuum map, showing the most prominent emission lines [O III], [N II], H_{α}, and [S II]. Units for both colour bars are erg cm^{-2} s^{-1} Å^{-1}.
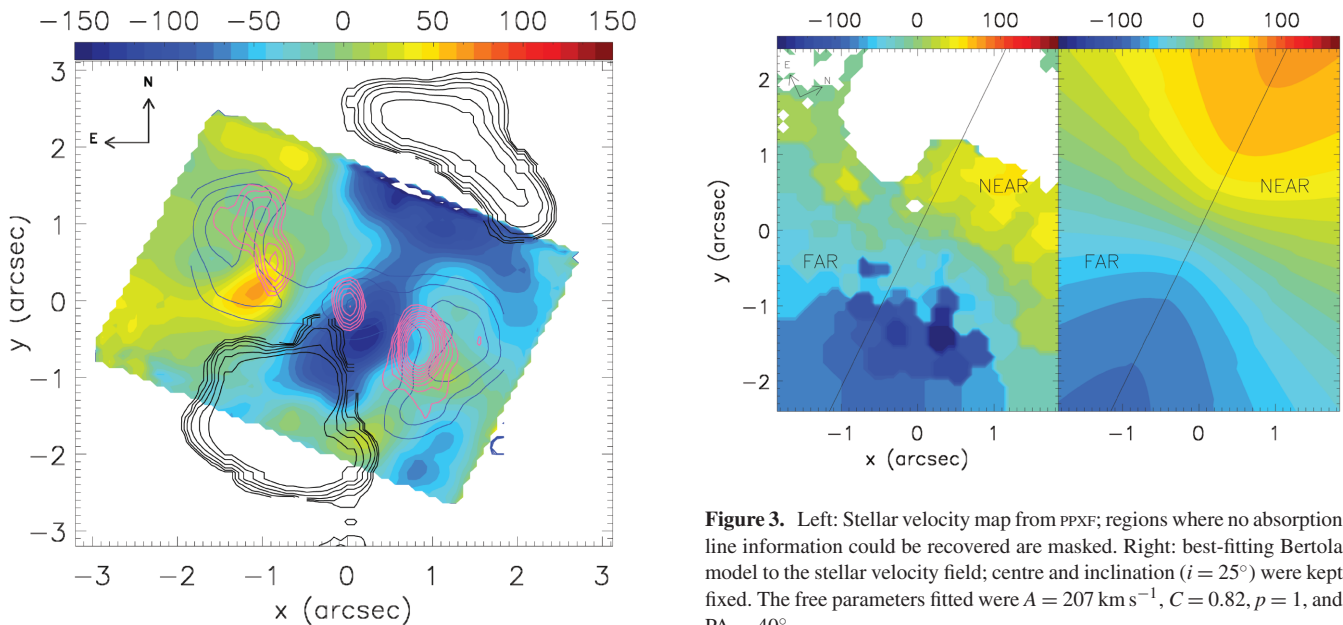
Figure 2. The moment 1 (velocity) map of the [N II] line from our GEMINI–GMOS/IFU observations is shown in colour following the colour bar at the top of the panel (scale in km s^{-1}). Blue contours indicate the moment 0 map of [N II], pink contours correspond to the VLA 8.4 GHz continuum map, and black contours show the moment 0 map from ALMA CO J:2-1 observations.

3 RESULTS

3.1 Stellar kinematics

The stellar kinematics was obtained from the absorption lines in the GEMINI–GMOS/IFU data cube. To model the stellar kinematics we

Figure 3. Left: Stellar velocity map from PPXF; regions where no absorption line information could be recovered are masked. Right: best-fitting Bertola model to the stellar velocity field; centre and inclination ($i = 25°$) were kept fixed. The free parameters fitted were $A = 207$ km s^{-1}, $C = 0.82$, $p = 1$, and PA $= 40°$.

used the penalized pixel-fitting (PPXF v5.2.1) routine developed by Cappellari & Emsellem (2004) and upgraded in Cappellari (2017), where the line-of-sight velocity distribution is recovered by fitting an optimized template to the galaxy spectrum. We used the INDO-US spectral templates library (Valdes et al. 2004). To reach the highest possible S/N to measure the stellar kinematics reliably, we spatially binned the data cube (S/N = 50) by using the Voronoi binning method described in Cappellari & Copin (2003). The spectra show no absorption lines in the region near the northern radio lobe: this region was thus masked before running PPXF.

The PPXF-derived stellar kinematic velocity map is shown in Fig. 3. Throughout this paper we adopt an inclination of 25° based on
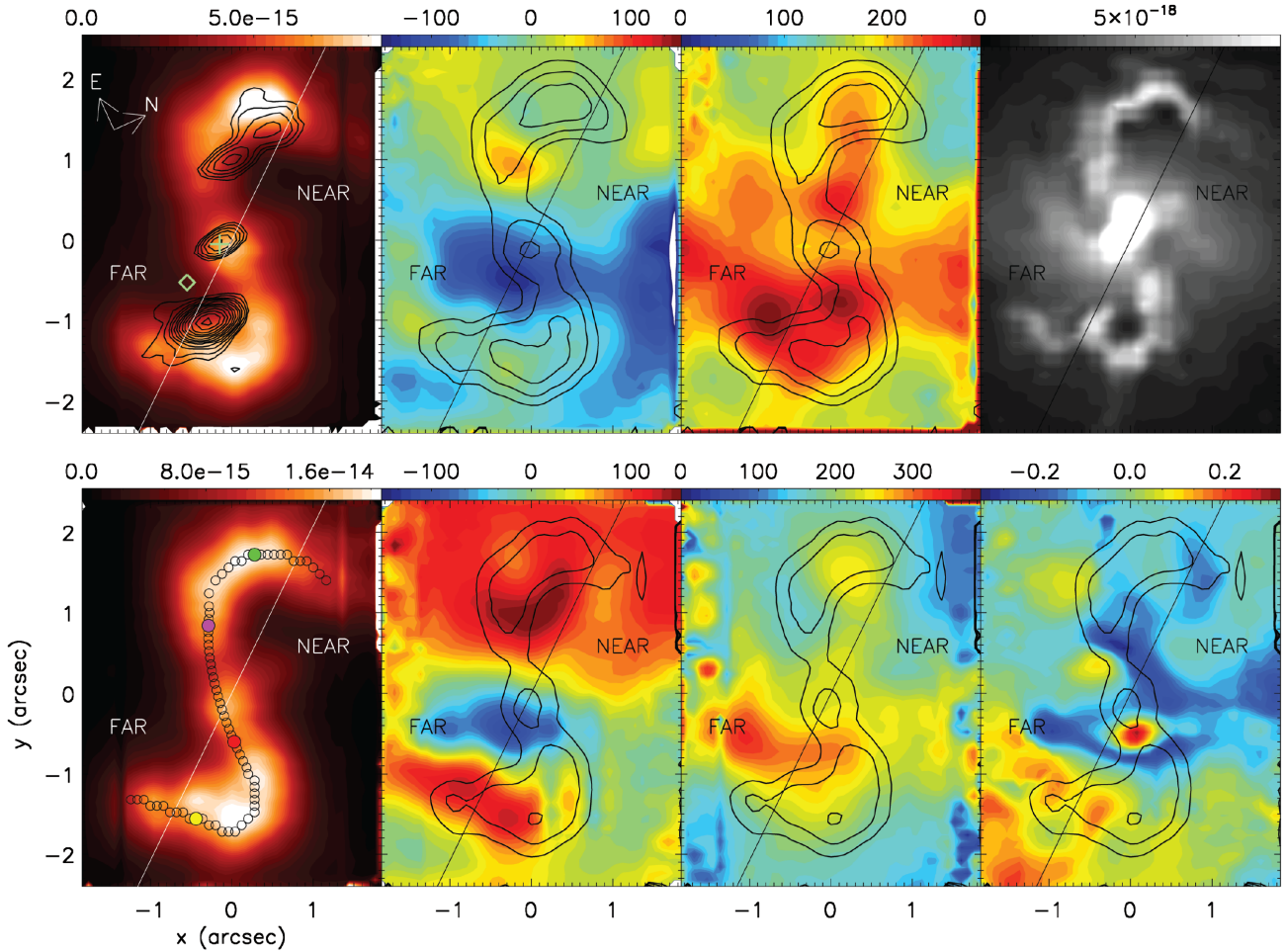
Figure 4. Moment maps for the [N II] λ6585 (top) and [O III] λ5007 (bottom) emission lines. First column: integrated flux, second: velocity map, third: velocity dispersion. The fourth column shows the structure map (top) and the h3 moment (bottom) from a one-component Gaussian–Hermite fit to the [O III] emission line; this moment represents the asymmetric deviations from a Gaussian profile. Black contours superposed on the moment 0 map of the [N II] line correspond to the VLA 8.4 GHz continuum map. Black contours in the moment 1, 2, and 3 maps correspond to the moment 0 of the respective line. Black circles in the moment 0 map of the [O III] line (bottom left corner) show the apertures positions along an S-shaped slit used to extract the position–velocity diagram shown in Fig. 5, the coloured apertures mark specific regions that can be identified in the pv-diagram. The galaxy major axis (PA 40°) is marked as a black line, delimiting the near and far side. The compass shown on top left corner shows the orientation of our GEMINI-GMOS/IFU data. The green cross marks the position of the stellar continuum peak, which we assume to trace the position of the nucleus. The green diamond shows the position of the SW secondary BH reported by Fabbiano et al. (2011). Colour bar units for moment 0 maps and structure map are erg cm^{-2} s^{-1} Å^{-1} for, km s^{-1} for moments 1 and 2, and unitless for h3 moment.

the axis ratio $a/b = 1.1$ (v1.10, de Vaucouleurs et al. 1991). We model the stellar velocity field obtained from PPXF using a spherical potential with pure circular rotation, assuming that the kinematical centre is cospatial with the peak in the continuum emission. The observed radial velocity from this potential is given by (Bertola et al. 1991)

$$V = V_{sys} + \frac{AR\cos(\psi - \psi_0)\cos^p\theta}{(R^2[\sin^2(\psi - \psi_0) + \cos^2(\psi - \psi_0)] + c^2\cos^2\theta)^{p/2}},$$

where V_{sys} is the systemic velocity, R is the radius, θ is the disc inclination, ψ_0 is the PA of the line of nodes, A is the amplitude of the rotation curve, c is the concentration parameter regulating the compactness of the region with a strong velocity gradient, and p regulates the slope of the 'flat' portion of the velocity curve. We perform a least-squares minimization using the IDL routine MP-FIT2DFUN (Markwardt 2009) to obtain the best-fitting parameters. The resulting model is shown in Fig. 3, where we kept centre and inclination (25°) fixed, and the free parameters of the fit and the

best-fitted values were $A = 207\,\mathrm{km\,s^{-1}}$, $c = 0.82$, $p = 1$, and $\Psi_0 = 40°$.

3.2 Ionized gas

To model the ionized gas emission in the GMOS-IFU data we use custom IDL routines. We begin our analysis by generating moment images for the most prominent spectral emission lines, [O III] λ5007 and the [N II] λλ6549, 6585 doublet. These moment images are created by collapsing one axis of the data cube.

The moment zero, i.e. integrated flux maps (Fig. 4) show an S-shaped morphology of the ionized gas, where two arm-like features leave the centre as a straight line along PA 55° and then curve, to the NW in the NE arm, and to the SE in the SW arm. The brightest emission is observed within an opening angle of 90° from the nucleus. The black contours in the [N II] moment zero map (Fig. 4) correspond to the 8.4 GHz VLA map, and indicate that the gas in

the S-shaped arms seems to surround both NE and SW radio lobes. This morphology, and the interaction between radio jet and ionized gas, was previously observed and analysed by Cooke et al. (2000) and Maksym et al. (2017).

Moment one, i.e. velocity maps, are shown in the second column of Fig. 4, where a gradient can be observed from NE to SW. However, given the complex kinematics of the NLR a precise determination of its PA is not possible using this moment image. Two high-velocity features are found to the NE and SW of the nucleus. The moment one map for the [O III] emission line shows that a redshifted component covers a large fraction of the FOV. For the [N II] line we observe that the NE region shows larger redshifts with increasing distance from the nucleus. However, with the exception of the blueshifted blob observed S of the nucleus, the SW region is not as blueshifted as expected from an inclined disc in pure rotation.

The moment two (velocity dispersion) maps, shown in the third column of Fig. 4, presents a large dispersion in the central region, extending from the centre in a section along the minor axis (referred to as the equatorial region hereafter), and a second high dispersion area is seen in the inner part of the NE arm. The dispersion is higher for the [O III] emission line.

The moment 3 (h3) map (bottom-right corner in Fig. 4) obtained from a one-component Gaussian fit, describes asymmetric deviations from a Gaussian profile, presents some skewness in the equatorial region, where negative values are indicative of a blueshifted wing or component. A large area in the SE region present a positive skewness, which indicates a strong redshifted wing or component. Similar distributions were observed for all moment maps of all strong emission lines fitted with a single Gaussian using PROFIT ([S II], H α, H β, [O I]; not shown).

To better examine the kinematics we defined a curved 'slit' that closely follows the S-shaped arms seen in the emission lines: the aperture positions of this slit are shown in Fig. 4 (bottom left-hand panel) and the position-velocity (pv) diagrams of the H α and [N II] lines, extracted from these apertures are shown in Fig. 5. The pure rotation model fitted to the stellar kinematics is shown as the solid black line. While we do see some gas at velocities close to this model, there are large deviations from the model which indicate the presence of multiple kinematic components. To guide the eye specific apertures along the slit are coloured (Fig. 4), and the pv-diagram is marked with a corresponding colour line at this aperture. The yellow and red apertures are near the SW radio lobe, while the magenta and green line apertures are near the NE radio lobe. The apertures near the yellow vertical line reveal gas that appears to follow the pure rotation model plus a redshifted wing with velocities reaching 500 km s^{-1}; no equivalent blueshifted wing is observed. In the apertures near the red vertical line we see little to no gas following the rotation model: instead we observe strongly blueshifted emission with velocities near −400 km s^{-1}. Apertures near the magenta line show a small fraction of gas following the rotation model, and a dominant component of gas is redshifted by up to ∼300 km s^{-1}. Apertures near the green line show a highly broadened profile: while the median velocity is roughly close to the rotation model, we see large (±300 km s^{-1}) redshifted and blueshifted velocities. In this region, an additional extreme redshifted component is observed, most clearly seen in the [N II] λ6585 line: this weak redshifted wing reaches velocities of 1000 km s^{-1}. Similar characteristics are observed in the pv-diagram of the [O III] emission line (not shown).

The kinematics of NGC 3393 were classified as turbulent by Fischer et al. (2013), based on *HST* spectroscopy, since they could
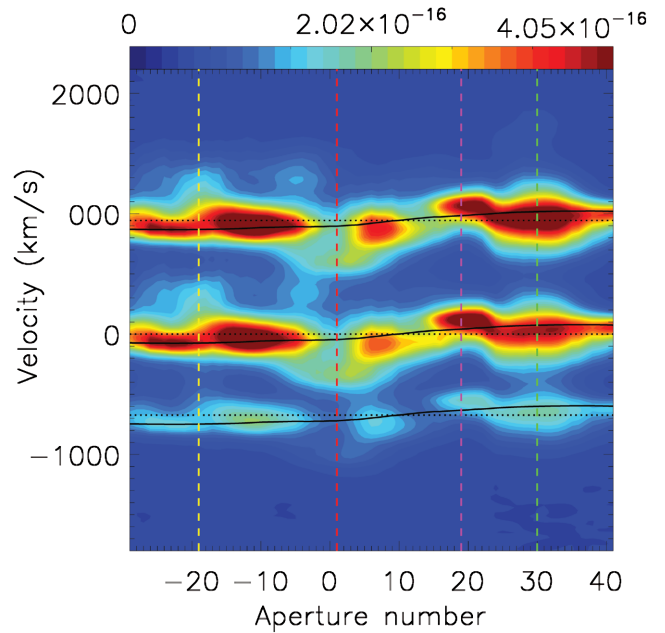

Figure 5. Position–velocity diagram of the continuum-subtracted GEMINI–GMOS/IFU data cube, centred on the H α emission line, extracted along the S-shaped 'slit' shown on bottom right-hand panel of Fig. 4. The solid black line shows the expectations of the Bertola rotation model derived from the stellar kinematics. For reference, vertical yellow, red, magenta, and green lines show the position of specific apertures that are marked with the same colours in Fig. 4 (bottom left corner). The dashed black lines show the zero-velocity for each emission line. Colour bar units are ergs cm^{-2} s^{-1} Å^{-1}.

not be satisfactorily fitted with a biconical outflow model. Given the complex kinematics of the NLR, the large velocity dispersion, the Gaussian skewness observed in the equatorial region, the multiple kinematical components observed in the pv-diagram, and a visual inspection of the spectra in the mentioned areas , the need for a multiple-component Gaussian fit is clear.

A visual inspection of the emission line profiles for the [O III], H α, and [N II] lines show a large difference of shape and width of the profiles in different regions of the FOV. To understand this difference we use the measurements described in Whittle (1985), where velocity widths are measured at some fraction of the cumulative line flux, the integral nature of these measurements makes them relatively insensitive to the nature of the profiles. For every spaxel we calculated: (a) **W80**, a line width parameter which measures the velocity width that encloses 80 per cent of the total flux. This parameter does not discard information of broad wings. (b) **A**, an asymmetry parameter as defined in Liu et al. (2013), where a symmetric profile will have a value of A = 0, and the presence of redshifted (blueshifted) wings will give a positive (negative) value. (c) **K**, a shape parameter that is related to the line kurtosis, for a Gaussian profile K = 0, while profiles that have broad wings will have K > 1 and stubby profiles will have K < 1. The values obtained for these parameters for the [O III] emission line are shown in Fig. 6. We use these results to identify spaxels in the FOV for which multiple component fits are required and factible. We consider pixels for which W80 > 350 km s^{-1}, A > 0.1 or A < −0.1, and K > 1.1 or K < 0.8, we created a mask by weighting the values for W80, A and K, to 80, 20, and 20 per cent respectively. Furthermore, regions with low S/N are masked out as the profiles are not as reliable. This mask contains the spaxels that require two Gaussian fits. Visual inspection of the maps show considerable larger values
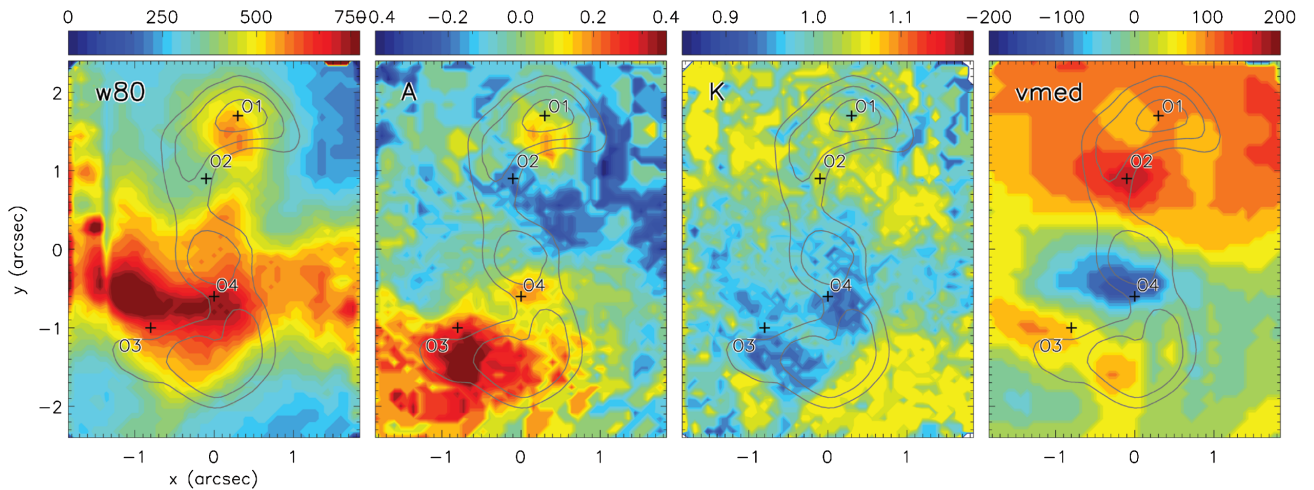
Figure 6. Profile measurements for emission line profiles described in Liu et al. (2013) and Whittle (1985). From left to right: W80 (velocity width that encloses 80 per cent of the total flux), A (asymmetry of the profile parameter), K (shape of the profile parameter), and V_{med} (median value of the integrated flux profile). For W80 and V_{med} the colour bar is in km s^{-1}, while A and K are unitless parameters. Grey contours correspond to the [N II] moment 0 map. Labels 'O1', 'O2, 'O3', and 'O4' correspond to areas of interest, explained in Section 3.2.

for W80 in some areas. For this area we consider the possibility of a three Gaussian component fit, and thus we made a second mask for regions where W80 > 500 km s^{-1}.

For the multicomponent analysis we use a custom IDL routine based on the routine PROFIT (Riffel 2010), fitting multiple Gaussian profiles to the emission lines of the GMOS-IFU spectra. We performed a two and three component Gaussian fit to the emission lines. We use a narrow component ($\sigma < 115$ km s^{-1}), a broad redshifted component ($115 < \sigma < 230$ km s^{-1}), and a third broad blueshifted ($115 < \sigma < 230$ km s^{-1}) component, based on the masks described above. Note that the 'broad' nomenclature used here should not be confused with the broad component typical of a Type 1 AGN.

The result of the multiple-component fit is shown in Fig. 7. To fit the narrow component we use as a first guess for each spaxel the velocity predicted by the pure rotation model fitted to the stellar kinematics, this component traces, more or less, gas rotating in a disc, with a kinematic major axis in PA 40° [this value is in agreement with the 37 ± 3° obtained by Cooke et al. (2000)]. From the moment zero maps it can be observed that this component is weaker for the [O III] line which seems to be more dominated by the broad red and blueshifted components. The broad redshifted components trace more complex kinematics that seem to be closely related to the radio jets. We have marked four areas of more interesting kinematics (regions marked 'O1', 'O2', 'O3' and 'O4' labels in Fig. 7). These areas coincide with the coloured vertical lines we used in the pv-diagram. The 'O1' area, as we observed in the pv-diagram, has a broad profile that is slightly asymmetric (top left-hand panel on Fig. 8), however no clear multiple peaks are observed and the separation between model and disturbed gas is not clear. A very broad weak redshifted wing is also observed in this area. The regions 'O2' and 'O3' seem to be outflow dominated and have strong high-velocity redshifted emission and appear to be closely related to the NE and SW radio lobes respectively. The 'O4' area shows the widest profiles observed in the FOV (bottom right-hand panel in Fig. 8), where three clear peaks are observed, the dominant component is the blueshifted emission, followed by a component that seems to follow rotation on the disc, and a weaker redshifted wing. This profile extends along a region perpendicular to the radio jet axis.

3.3 Molecular gas: CO J:2-1

To illustrate the distribution of the molecular gas relative to the other components of the galaxy we show in Fig. 9 both the CO J:2-1 (ALMA; cyan) and [N II] (GEMINI-GMOS/IFU; black) integrated flux maps overlaid on an *HST* F606W image to which we applied an unsharp-mask filter, with the goal of emphasizing structures, such as dusty regions (we refer to this filtered image as 'structure map' from now on). It can be observed that the ionized and molecular gas barely overlap, due to the limited FOV of our GMOS-IFU data, this can be observed better in Fig. 2. There is little to no CO J:2-1 molecular gas observed in the central region. This implies either a true lack of molecular gas or is a critical density effect, that is, the gas density may be high enough that the CO J:2-1 transition is collisionally, rather than radiatively, de-excited. The outer distribution of CO J:2-1 seems to follow the inner ring-like structure, where the structure map shows the presence of dust. The observed molecular gas morphology in the nuclear region could be a result of the molecular gas and radio jet interaction: the latter can produce entrainment of the gas along the jet PA, and push gas away from the centre perpendicular to this PA. Alternatively, the molecular gas density is high enough that the CO J:2-1 transition is 'dark' and a dense molecular gas tracer is required.

The CO J:2-1 moment 0 map is shown in Fig. 10: the distribution of the molecular gas is fragmented and does not cover a large fraction of the FOV. The SE component close to the centre is the region with the brightest CO J:2-1 emission. The outer region shows large-scale spiral arms that broadly resemble a ring. There is some emission present in the region between the SE component and the outer arms.

Fig. 10 presents the CO J:2-1 moment 1 map. We classified the kinematics in two regions, an inner region inside a circle of 5 arcsec (marked in grey in Fig. 10) and an outer region, outside this circle. We can see a gradient in velocity from NE to SW in the outer distribution of gas, as it is expected for gas rotating in the disc. However, in the inner region the kinematics does not follow the outer region's rotation: in the SE inner component there seems to be a gradient of velocity in PA −45°, and the NW inner component shows mainly blueshifted velocities.
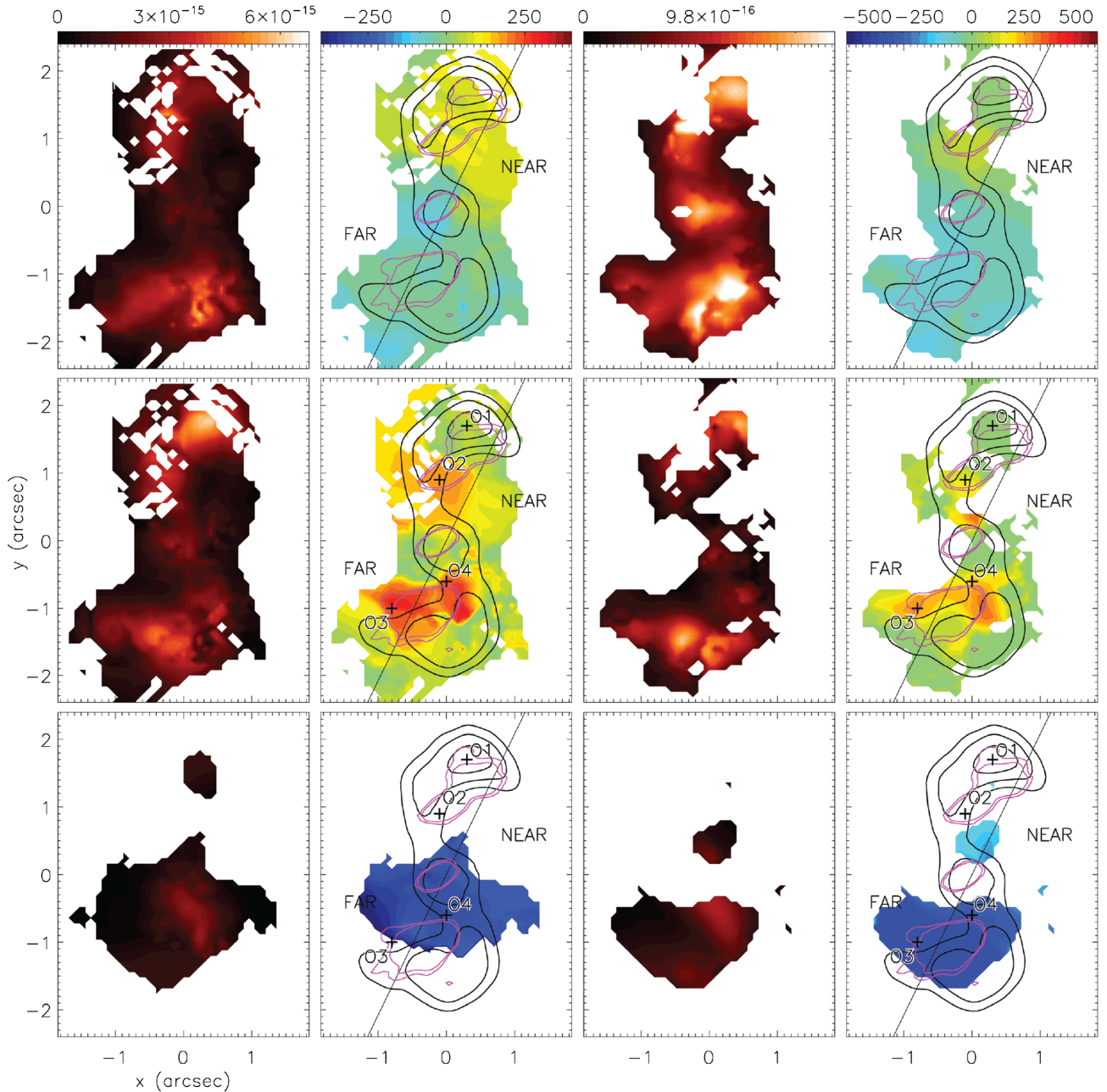
Figure 7. Moment 0 and 1 maps from our multiple-component Gaussian fits to the [O III] and [N II] emission lines. First and second column show the moment 0 and moment 1 map for the [O III] line. Third and fourth column show the moment 0 and 1 for the [N II] line. First, second and third row show the narrow, broad redshifted, and broad blueshifted components respectively. Crosses marked as 'O1', 'O2', 'O3', and 'O4' show the areas of interest defined in the text. Black contours in the moment 1 maps show the moment 0 map of the corresponding emission line, obtained from the axis collapse, as shown in Fig. 4. Pink contours correspond to the VLA 8.4 GHz map. Units for the moment 0 maps are erg cm^{-2} s^{-1} Å^{-1}, and km s^{-1} for the moment 1 maps.

We model the kinematics in the outer region with a pure circular rotation model obtained from an exponential disc potential, defined by

$$\Phi(R, z) = -2\pi G \Sigma_0 r_d^2 \int_0^\infty \frac{J_0(kR)e^{-k|z|}}{[1 + (kr_d)^2]^{3/2}} dk \, ,$$

where (R, z) are cylindrical coordinates, G is the gravitational constant, Σ_0 is the central surface brightness, r_d is the disc scale length, and J_0 is the zeroth order cylindrical Bessel function. For this model we assume an infinitesimally thin disc $(z \to 0)$. The rotation velocity

from this potential is given by

$$V_{\text{ROT}}^2(R) = R \frac{\partial \Phi}{\partial R} \, .$$

We perform a least-squares minimization (using the MPFIT2DFUN routine in IDL) to obtain the parameters that are best fitting the observed CO J:2-1 velocity field (Fig. 11). The PA cannot be well constrained due to the scarcity of the data along the major axis, we thus fix the major axis PA to 40° (See Section 5) after verifying that the velocity profiles of the CO J:2-1 along, and near, the minor axis is most consistent with this major axis PA (e.g. fig. 12), and also
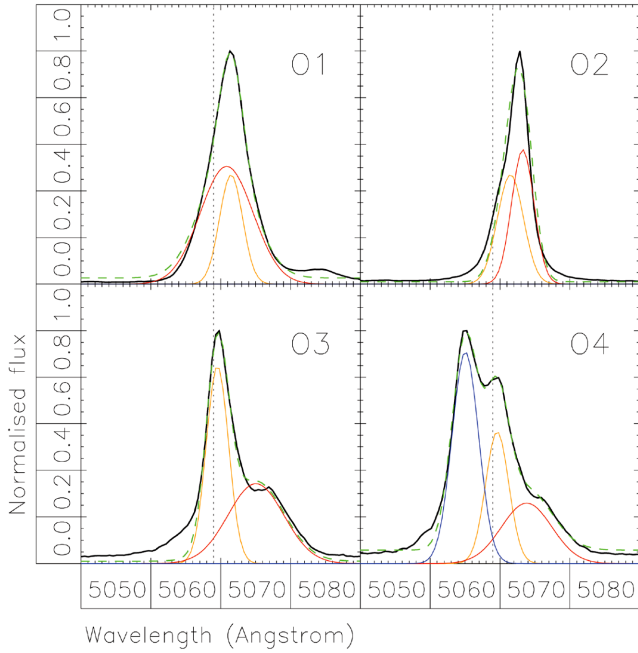
Figure 8. Examples of multiple-component Gaussian fits to the [O III] emission line in the 'O1', 'O2', 'O3', and 'O4' areas shown in Fig. 7. The narrow, broad redshifted, and broad blueshifted components are shown in yellow, red, and blue, respectively, and their sum is shown by the dashed green line. Dotted vertical line shows systemic velocity.
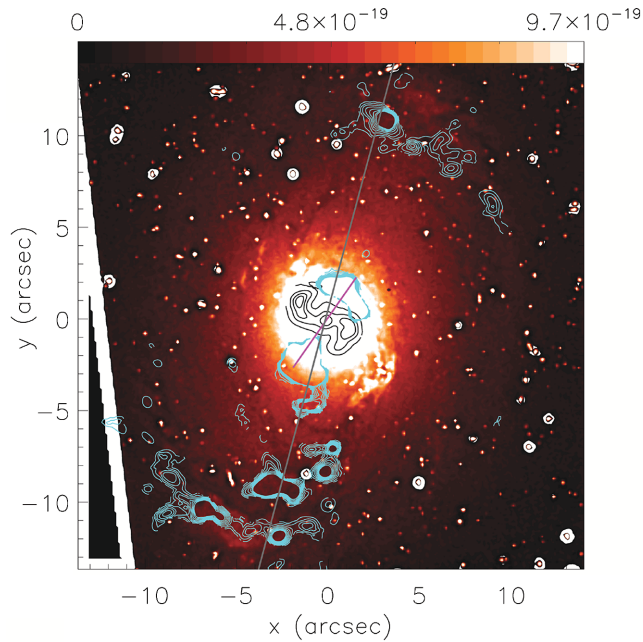

Figure 9. The structure map (obtained using a F606W *HST* image) of NGC 3393 is shown in colour, with overlays of the ALMA CO J:2-1 moment 0 map (cyan contours) and the GMOS [N II] moment 0 map (black contours). The grey line marks the PA of the large-scale bar, and the magenta line corresponds to the PA and estimated extension of the nuclear bar. Colour bar units are $\mathrm{ergs\,cm^{-2}\,s^{-1}\,\mathring{A}^{-1}}$.
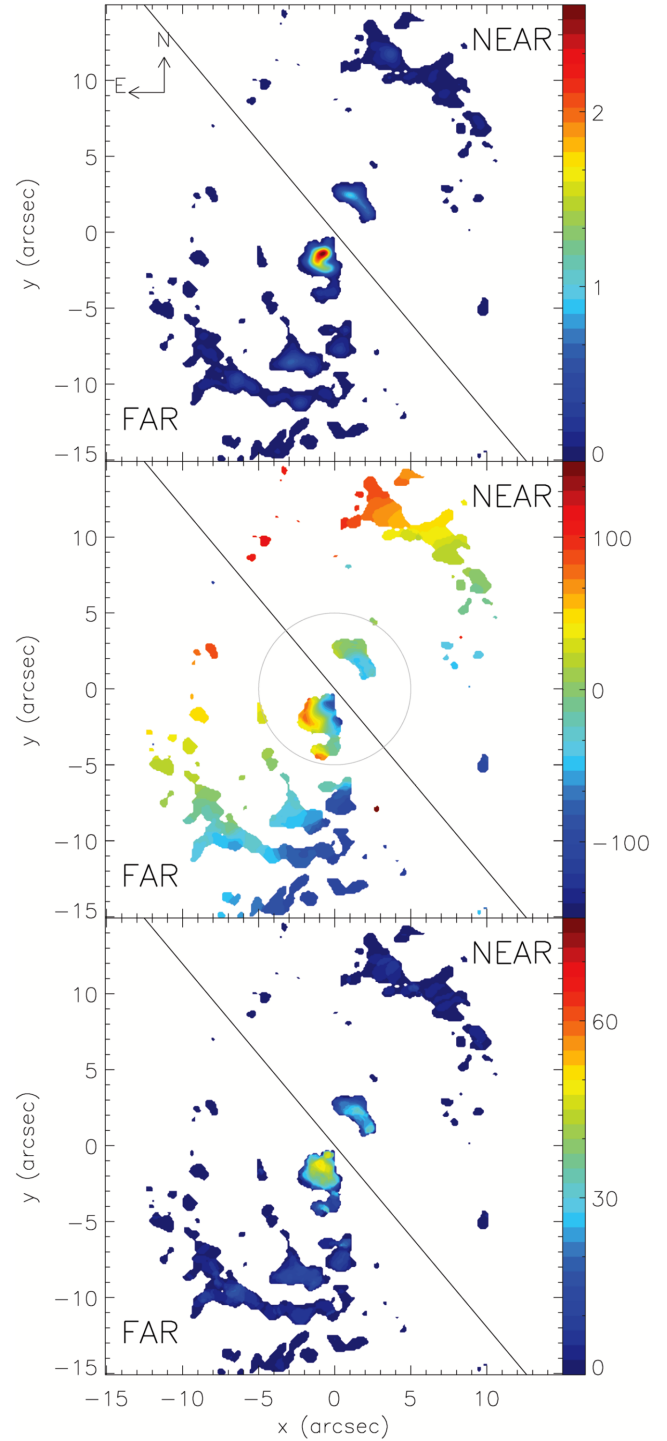

Figure 10. Moment maps for ALMA CO J:2-1 data. Top: integrated flux (moment 0) map following the colour bar (units of $\mathrm{Jy\,beam^{-1}}$). Middle: velocity map (moment 1) after subtraction of a CO systemic velocity of $3746\,\mathrm{km\,s^{-1}}$; the grey circle separates the inner region and outer region referred to in the text. Bottom: velocity dispersion (moment 2) map. Moment 1 and 2 colour bar units are $\mathrm{km\,s^{-1}}$. In all panels N is up and E is to the left, and the black line marks the adopted major axis PA of $40°$.
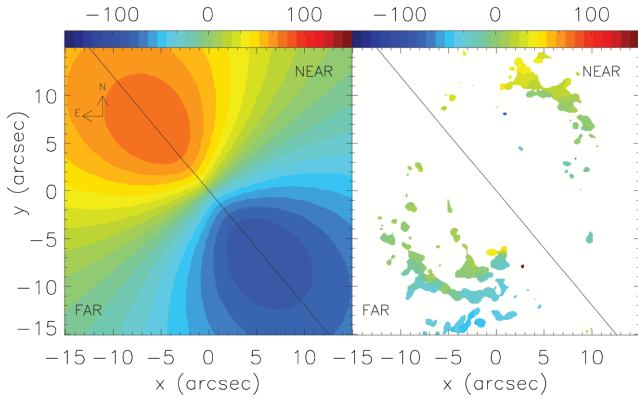
Figure 11. Left: Our pure rotation model derived from fitting the outer (outside the grey circle in Fig. 10) CO velocity field with a model based on an exponential disc potential (see text). Right: residual (observed model) velocity field of the outer disc.
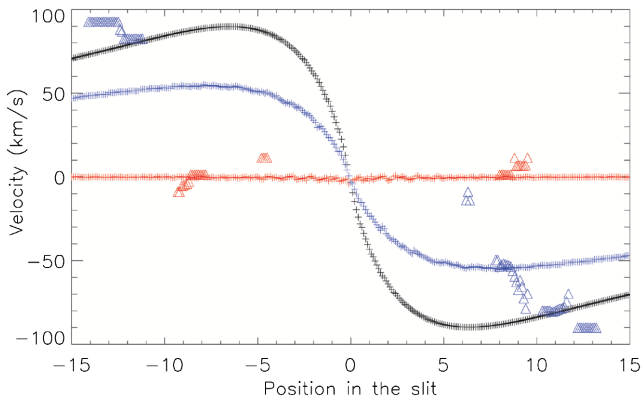

Figure 12. CO J:2-1 rotation curves in the outer (outside the grey circle in Fig. 10) region along the major axis, minor axis (red triangles), and PA 10° (blue triangles). Plus symbols show the best-fitted pure rotation exponential disc model along the same PAs.

fix the inclination to $i = 25°$. Based on the rotation curve along the minor axis, we use a -26 km s^{-1} offset from the systemic velocity ($V_{sys} = 3746$ km s^{-1} from HI Parkes All Sky Survey; Meyer et al. 2004), to better fit the CO J:2-1 data. For the free parameters r_d and M_d, the mass and scale length of the disc respectively, the best-fitted values obtained are $r_d = 1$ kpc and $M_d = 2.7 \times 10^{10}$ M$_\odot$. For comparison, the values obtained by the *HST* light distribution modelling of Läsker et al. (2016) are $r_d = 1.38$ kpc and $M_d = 2.04 \times 10^{10}$ M$_\odot$. The resulting exponential disc model and the residual from the model subtraction to the CO J:2-1 velocity map are shown in Fig. 11. The rotation curves of the CO J:2-1 and the exponential disc model are shown in Fig. 12.

The velocity dispersion (moment 2) map is shown in the rightmost panel of Fig. 10: the highest values are observed in the inner region, with the highest dispersion found in the SE component. Example spectra of this region can be found in Fig. 13.

The pv-diagram taken along a slit of PA $-50°$ (Fig. 14), centred on the SE feature, shows a clear gradient in velocity along the SE feature. A second pv-diagram extracted along the minor axis, centred on the galaxy centre, using a natural weighted, four-channel averaged image (10 km s^{-1}) is shown in Fig. 14. The clear gradient
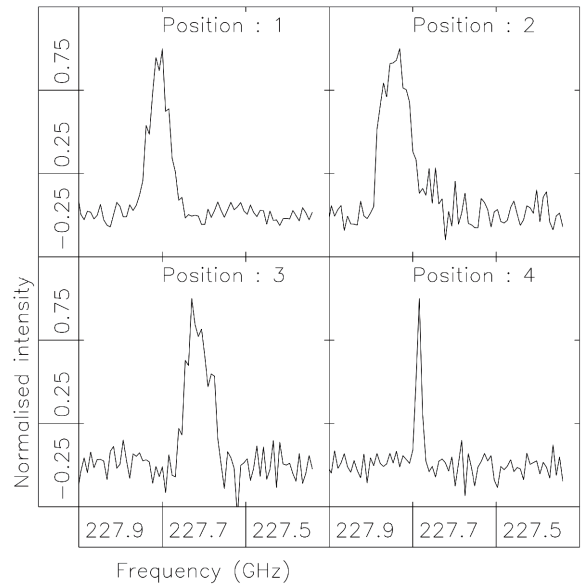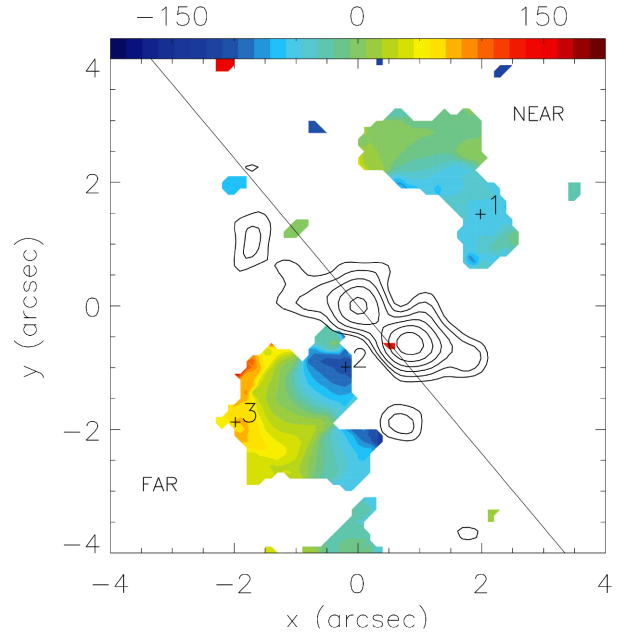

Figure 13. Top: observed CO J:2-1 velocity field of the inner region is shown in colour following the colour bar (units of km s^{-1}). Black contours show the ALMA 230 GHz continuum map. Bottom: example CO J:2-1 spectra of three distinct positions (1–3) in the inner SE feature as identified in the left panel, plus, for comparison, the spectrum of a fourth position (4) located outside the inner region.

of the SE component seems to follow a PA close to the minor axis, and to the PA of the nuclear bar (Fig. 9). The unusual kinematics of this inner region is addressed in Section 4.2.2, where we argue that it is a possible result of the interaction between the large-scale bar and the nuclear bar.

A map of the 230 GHz continuum (close to the CO J:2-1 emission line, Fig. 13) shows three components whose positions closely corresponds to the nucleus and radio lobes observed in the VLA 8.4 GHz data (see tables 2 and 3 of Koss et al. 2015). The 230 GHz total fluxes are 0.2 mJy for the nuclear source, 0.31 mJy for the SW
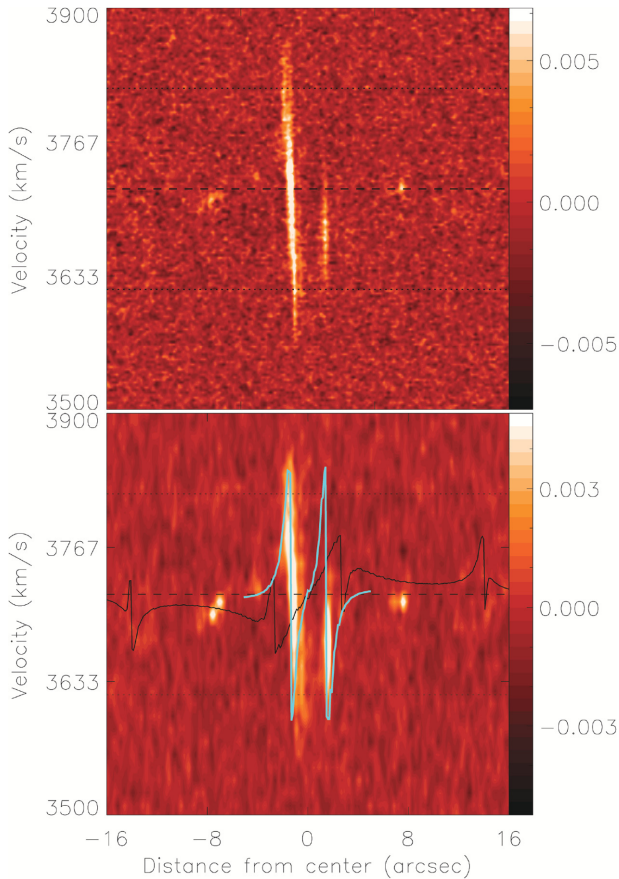
Figure 14. Top: pv-diagram centred on the SE component in the CO maps, extracted along a PA of −50°. Bottom: pv-diagram extracted from a natural weighted, four-channel averaged cube with 10 km s⁻¹ spectral resolution, with a slit centred on the galaxy nucleus and extracted along the minor axis. The black line shows the prediction of the large-scale bar perturbation model described in Section 4.2.1 and the blue line shows the prediction of the nuclear bar model. Colour bar units are Jy beam⁻¹.
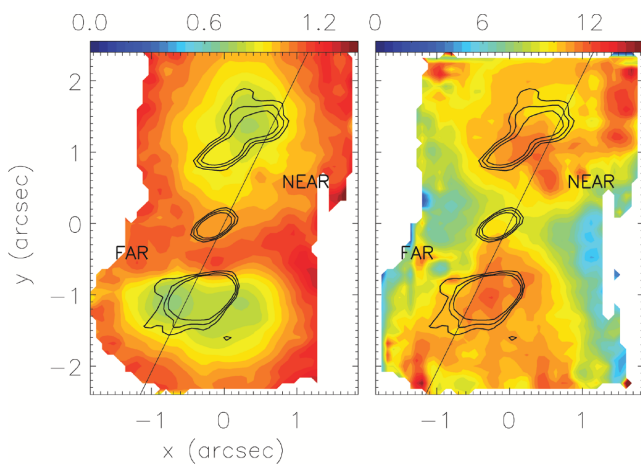

Figure 15. Left: [S II] λ6716/λ6731 line ratio map. Right: [O III]/Hβ line ratio map. Black contours correspond to the VLA 8.4 GHz map. The major axis of the galaxy (PA = 40°) is shown with the black line.

source, and 0.08 mJy for the NE source. Given the match in position of the three components observed in the milimetre continuum with the radio lobes observed in the VLA 4.9–8.4 GHz emission, and that the observed 230 GHz fluxes are in close agreement with the extrapolation of the 8.4 GHz fluxed and the 4.9–8.4 GHz spectral indices, we conclude that these are the same components as those observed and analysed in detail by Koss et al. (2015).

4 DISCUSSION

The main nuclear radio features of the galaxy are the nuclear component, with a flat spectrum, and two hotspots, NE (∼2 arcsec) and SW (∼1 arcsec) from the nucleus, with a steeper spectra, indicative of a two-sided jet. The larger flux in the SW lobe is attributed to Doppler boosting by Koss et al. (2015), assuming that the NE component is receding and the SW is approaching. There are no other previous studies that allude to the jet position in the galaxy in greater detail.

Based on the kinematics presented here, the edge-on maser disc with extension ∼1 pc in PA perpendicular to both the jet axis and the major axis of the galaxy, and the relatively low inclination of the galaxy disc (as compared to the maser disc), we interpret the jets as being launched into the disc of the galaxy. The SW lobe may represent the point where the radio jet leaves the disc of the galaxy. This scenario implies a maximum interaction between the radio jet and the dense gas in the galaxy disc.

The S-shaped morphology and the possible origin of these arms have been discussed in detail in Cooke et al. (2000) and Maksym et al. (2017), where radial jet motion, entrainment of patterns in the ISM, and accretion disc precession have been suggested as possibilities. Maps of gas excitation (as traced by the [O III]/Hβ ratio) and density (high ratios of [S II] λ6716/λ6731 denote higher densities) are shown in Fig. 15. The region of higher gas excitation appears to be biconical, centred on the nucleus, in PA ∼50°, and with an opening angle of 45°. This conical morphology is most obvious to the SW. Similar morphologies can be observed in the line ratio maps of [O III]/Hα, and [S II]/Hα, where the ratio is lower inside the bicone, and higher outside, which indicates possible shocks and lower photoionization outside the cones. However, giving that the profiles of the Hα line is blended with the [N II] doublet in the areas where the kinematics are more complex, the maps produced are not as reliable as that of [O III]/Hβ. Despite this, the general biconical shape, with high excitation inside the cones, is maintained but the specific values for the line ratios can change depending on the Gaussian fit or spectral window used to obtain the flux of the lines. Similar results, with Seyfert-like emission inside the biconical shape that encloses the S-shaped arms and low-ionization nuclear emission-line region-like emission outside the S-shaped arms, has been found by Maksym et al. (2017). It is thus likely that an ionization cone is present in the galaxy along a PA ∼50° and with an inclination similar to the galaxy inclination. However, the gas illuminated in this ionization cone has kinematics that is most likely dominated by radio jet interactions with the gas in the FOV of our GMOS/IFU data. As shown in Cooke et al. (2000) a high-excitation gas region extends to ∼20 arcsec and thus a larger FOV will help to constrain the presence and characteristics of this ionization cone.

4.1 Outflows

The masking and multicomponent Gaussian fit to the [O III] emission line discussed in Section 3 shows four areas of interest that we

have labelled 'O1', 'O2', 'O3', and 'O4' (Fig. 7). The 'O1' region is 1″8 NE of the nucleus, near the NE radio lobe. The spectrum of this region shows a wide profile ($\sim$500 km s^{-1}) which we have fitted with the broad redshifted component. However, both the broad redshifted component and the narrow component, which follows the expectations of rotation in the galaxy disc, have a similar velocity, and thus we do not consider a flow of gas in this region. The [S II] $\lambda6716/\lambda6731$ line ratio map shows an area of larger electron density near the 'O1' region (Fig. 15), which can indicate that shocks are being produced by the interaction between the radio lobe and the ionized gas.

The 'O2' region, near the NE radio lobe, shows a wide profile that seems to have multiple components present (Fig. 8) and is fitted by a narrow component and broad redshifted component; this broad component shows velocities redshifted $\sim$180 km s^{-1} from systemic velocity. We consider this to be an outflow produced by the radio jet in the plane of the disc. The 'O3' region, near the SW radio lobe, shows a profile with a clear broad, redshifted wing. We fitted this profile with a narrow component that seems to be following the rotation of the disc, and a broad redshifted component, this broad component is redshifted $\sim$200 km s^{-1} from systemic velocity. We consider this redshifted emission to be an outflow produced by the radio jet in the plane of the disc.

The 'O4' area shows the widest profiles ($\sim$700 km s^{-1}) observed in our FOV and clearly shows three different components, which we fitted with three Gaussian profiles: narrow, broad redshifted, and broad blueshifted components. This area extends between the nuclear and SW radio components, and along the equatorial region (that is, perpendicular to the radio jet and nuclear maser disc rotation axis). This region shows a lower electron density (Fig. 15) and high-velocity blueshifted emission is observed along the area, while redshifted emission is observed on a more concentrated subsection of the area, closer to the SW radio lobe. We interpret this to be an equatorial (with respect to the central engine) outflow.

In the following sections we will discuss the NE ('O2') and SW ('O3') jet-driven outflows, and the equatorial outflow ('O4') in more detail.

4.1.1 Jet-driven outflow

To estimate the ionized gas outflow rate we estimate the mass of the gas and the velocity of the outflow, following Lena et al. (2015a). The gas mass is given by

$$M_{\mathrm{g}} = N_{\mathrm{e}} m_{\mathrm{p}} V f, \tag{1}$$

where N_{e} is the electron density, m_{p} is the proton mass, V is the volume considered, and f is the filling factor, which can be estimated by

$$L_{\mathrm{H}\alpha} \sim f N_{\mathrm{e}}^2 j_{\mathrm{H}\alpha}(T) V, \tag{2}$$

where $L_{\mathrm{H}\alpha}$ is the H α luminosity emitted by the volume V, and $j_{\mathrm{H}\alpha} = 3.534 \times 10^{-25}$ erg cm^{-3} s^{-1} (Osterbrock 1989). Combining these two equations we obtain

$$M_{\mathrm{g}} = \frac{m_{\mathrm{p}} L_{\mathrm{H}\alpha}}{n_{\mathrm{e}} j_{\mathrm{H}\alpha}(T)}. \tag{3}$$

To estimate the outflow rate we use an aperture of 0″6 for each component. For the 'O2' outflow, the mean [S II] $\lambda6716/\lambda6731$ line ratio of the broad redshifted Gaussian component is 0.92, which corresponds to an electron density of 740 cm^{-3}, the H α luminosity of the same Gaussian component in this aperture is 3.4×10^{40}

erg s^{-1}, and the gas mass that is outflowing, assuming a luminosity distance to the galaxy of 52 Mpc, is 11×10^4 M$_\odot$; the mean deprojected velocity in the aperture is 180 km s^{-1}. This gives an outflow rate for 'O2' of $\dot{M} = 0.07$ M$_\odot$ yr^{-1}. For 'O3', the electron density is 980 cm^{-3}, the H α luminosity is 3.6×10^{40}, the mass is 9×10^4 M$_\odot$. The mean deprojected velocity is 210 km s^{-1}. Thus, the outflow rate for 'O3' is $\dot{M} = 0.06$ M$_\odot$ yr^{-1}.

4.1.2 Equatorial outflow

The [O III] multicomponent Gaussian fits shows the presence of a strong broad blueshifted component along the equatorial region, on a strip $\sim$1 arcsec wide along PA 147°. The velocity map of this component is shown in Fig. 7 (marked as 'O4') where high blueshifted velocities can be observed in the equatorial region, perpendicular to both the galaxy disc PA and the radio jet axis. The presence of a weak redshifted component can be inferred from a redshifted wing, visible on a compact fraction of the equatorial region (Fig. 7), and is not present on the entire equatorial region as the blueshifted component is. This distribution and the presence of a blue component in the region perpendicular to the radio jet axis indicates the presence of an equatorial outflow along PA 147°, which is in good agreement with the water maser disc PA, which is nearly perpendicular to the radio jet axis and extends for an $\sim$1pc Kondratko et al. (2008). In this scenario the redshifted component will be behind the galaxy disc and thus will appear weaker due to obscuration in the disc, as indicated in Cooke et al. (2000) the presence of a dust lane is observed in the central 0″5 of the continuum peak (*HST* f547m filter) along PA $\sim$115°, this dust lane is also observed by Pogge (1997) in the *HST* F606W. The interaction of a strong equatorial outflow from the accretion disc with the surrounding gas can push the ionized gas outwards.

Although the presence of outflows along the radio jet is more common (e.g. Das, Crenshaw & Kraemer 2007; Barbosa et al. 2009; Storchi-Bergmann et al. 2010), equatorial outflows have been included in theoretical models of accretion disc winds (Li, Ostriker & Sunyaev 2013), and outflowing torus models (Elitzur 2012; Hönig et al. 2013), and observationally found in NGC 5929 (Riffel, Storchi-Bergmann & Riffel 2014, 2015) and NGC 1386 (Lena et al. 2015b) where a distinct component that involves rotation and/or outflow extends to 2–3 arcsec ($\sim$ 200 pc) at either side of the nucleus, an extension similar to that found in NGC 3393.

In this scenario, and given that the galaxy is almost face-on, we assume that the blueshifted gas is in front and possibly leaving the disc and the redshifted gas is behind. The mean [S II] $\lambda6716/\lambda6731$ line ratio of the blue component in the equatorial region is 0.93 which corresponds to an electron density of 720 cm^{-3}. The H α luminosity of the region is 5×10^{40} erg s^{-1}. From equation (3) we obtain a mass of $M_g = 2 \times 10^5$ M$_\odot$, the mean observed velocity is -420 km s^{-1} and we consider this to be the true velocity of the gas, i.e. this outflowing gas is not in the plane of the disc, but leaving it, and approaching in the line of sight.

The estimated equatorial outflow rate, under these assumptions, is $\dot{M} = 0.24$ M$_\odot$ yr^{-1}. An alternative method to derive the equatorial outflow rate is to assume a hollow cylinder geometry that is expanding from the centre, with a height of 0″5. In this case the estimated outflow rate is 7 M$_\odot$ yr^{-1}, assuming a filling factor $f = 0.01$ (following Riffel et al. 2015). The differences in these two outflow rate estimates suggests the need of a filling factor closer to $\sim$0.001 or a significantly smaller height.
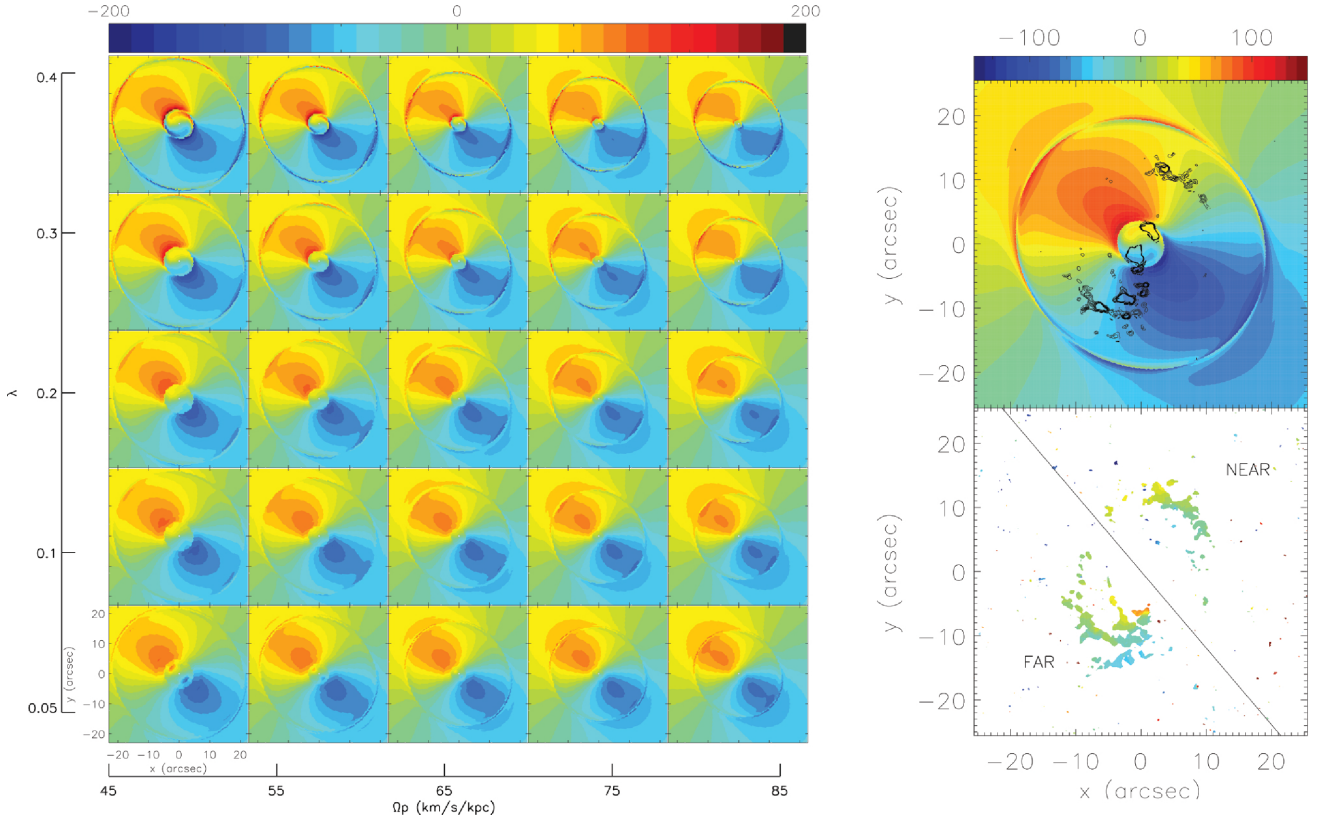
Figure 16. Left: Velocity fields resulting from the bar perturbation model described in Section 4.2, when varying $\Omega_{\rm p}$ (x-axis, values from 45 to 85 km s^{-1} kpc^{-1}, with a 10 km s^{-1} kpc^{-1} step), and λ (y-axis, values of 0.05, 0.1, 0.2, 0.3, and 0.4). All models use the intrinsic rotation curve derived from the best-fitting exponential disc model with parameters as explained in Section 3.3, and the bar parameters used were those of the large-scale bar: PA$_{\rm bar}$ = 160° and ϵ = 0.15. All panels follow the colour bar shown at the top (units of km s^{-1}). Top right: velocity field of the best-fitting bar perturbation model (see text) to the large scale (outside the grey circle in Fig. 10) CO velocity field following the colour bar above the panel (units of km s^{-1}). The values of the exponential disc parameters, disc PA, and inclination were fixed to the values outlined in Fig. 11, and the bar PA (PA$_{\rm bar}$ = 160°) and ellipticity (ϵ = 0.15) were set to the values of the large-scale bar. The best-fitting values for λ and $\Omega_{\rm p}$ are 0.1 and 54 km s^{-1} kpc^{-1}, respectively. Overlaid black contours show the integrated intensity (moment 0) of CO J:2-1. Bottom right: Residual (observed model) velocity map for the bar perturbation model following the colour bar above the panel (units of km s^{-1}): only the large-scale velocity residuals are shown.

4.2 Bar perturbations

To understand the role of the bar-induced perturbations to the molecular gas kinematic we have applied the harmonic decomposition formalism described in Schoenmakers, Franx & de Zeeuw (1997b) and Wong et al. (2004). It is important to remark that this formalism is based on linear epicycle theory, and thus it is only valid for weak bars, as the departure from circular orbits must be small compared to the circular velocity. The line-of-sight velocity towards a given point in a galaxy velocity field can be decomposed in a Fourier series as

$$V_{\rm LOS}(R) = c_0 + \sum_{j=1}^{n}[c_j \cos(j\psi) + s_j \sin(j\psi)] \sin i \,,$$

where (R, ψ) are polar coordinates, i is the inclination of the disc, c_0 corresponds to the systemic velocity ($V_{\rm sys}$), and j is the harmonic number. The coefficients c_j and s_j are a function of the circular velocity ($V_{\rm c}$), the bar pattern speed ($\Omega_{\rm p}$), ellipticity of the potential (ϵ), and the bar viewing angle ($\theta_{\rm obs}$), which corresponds to the bar PA from the minor axis of the galaxy disc (see e.g. fig. 2 of Wong et al. 2004, for a definition of this angle). A bar creates a bisymmetric gravitational potential which has a predominant m = 2 Fourier component, and thus we only consider the harmonics j

= m − 1 and j = m + 1 (Schoenmakers et al. 1997a). For the circular velocity ($V_{\rm c}$) we used the value obtained from the best-fitting exponential disc potential (Fig. 11 and Section 3.3).

A constant damping term (λ), simulating a radial frictional force, is introduced (e.g. Lindblad & Lindblad 1994; Wada 1994) to avoid sudden changes in orbit axes and thus multiple orbits at a given point. Usual values for this parameter are in the range of 0.05 < λ < 0.4.

For the case of NGC 3393, $\Omega_{\rm p}$ and λ are the parameters with the largest uncertainties. We thus build a library of models with different parameter combinations, a section of which is shown in Fig. 16, where the two parameters are varied over 0.01 < λ < 0.2 and 25 < $\Omega_{\rm p}$ < 85 km s^{-1} kpc^{-1}. The primary effect of changing $\Omega_{\rm p}$ is the variation in the radii of the resonances, but it also affects the magnitude of twists in the isophotes. The effect of increasing λ is to smoothen the sudden twists seen near the resonances.

We attempted to fit the full CO velocity field to this perturbation theory model, with $\Omega_{\rm p}$ and λ as free parameters, and the perturbations terms set by the large-scale bar PA and ellipticity. However, we could not find any suitable set of parameters (even if the bar PA was varied) which could match both the outer CO velocities and the highly perturbed velocities in the SE inner CO component. We

are thus forced to conclude that a single $m = 2$ (i.e. bar) mode is unable to explain the complex molecular kinematics seen in NGC 3393. The remaining option is thus to attempt to separately fit perturbations in the large-scale molecular kinematics (driven by the large-scale bar) and in the inner molecular kinematics (driven by the nuclear bar), which we do in the following subsections.

4.2.1 Large-scale bar

To obtain the (large-scale) bar perturbation model that best fits the outer CO kinematics we fit the observed CO velocity field (outside the grey circle in Fig. 10) to the predictions of our bar-perturbation models by using the same least-squares minimization routine as explained above, in order to obtain the best-fitted parameters. We fix the exponential disc model parameters to those obtained above. We also fix the ellipticity of the potential ($\epsilon = 0.15$) and the bar PA ($PA_{bar} = 160°$) to the values obtained for the large-scale bar by Jungwiert et al. (1997). The free parameters are thus the damping term (λ) and the bar pattern speed (Ω_p).

The resulting best-fitting model obtained and its velocity residuals are shown in Fig. 16. The rms of this residual map is lower than that obtained when only the pure rotational model of the exponential disc is used, though the difference is not large. To further test the suitability of the best-fitting model we compare the model with data extracted along the minor axis in the pv-diagram shown in Fig. 14. In the outer region, both model and data are close to zero as expected along the minor axis, however the model does not fit the data in the inner region, where the large velocity gradient of the SE feature is observed. This exercise shows that a bar perturbation model could maintain velocities similar to the exponential disc model in the outer region while having a different PA and velocity distribution inside the resonance radius.

The resonances observed in the best-fitted model correspond to the Inner Lindblad Resonance (ILR; at $r = 3.7$ arcsec), Outer Lindblad Resonance (OLR; $r = 20$ arcsec), an Corotation Resonance (CR; $r = 13.5$ arcsec) which is in good agreement with the length of the large-scale bar [SMA ∼13 arcsec according to Alonso-Herrero et al. (1998); Läsker et al. (2016)]. The ILR encloses the nuclear region, including both SE and SW features, and the OLR encloses the outer distribution of molecular gas. These two resonances could help explain the difference in PA of the ALMA and GMOS data compared to the large-scale kinematics PA (68°, according to Cooke et al. 2000). It is also interesting to note that the kinematics enclosed in the ILR resemble the observed stellar velocity map, specially the S-shaped zero velocity line (Fig. 3).

The primary limitation in the analysis above is the sparse filling factor of CO velocities over the FOV. Deeper integrations with ALMA are thus crucially required. Alternatively, deep observations of the ionized gas kinematics over the full galaxy (using e.g. VLT/MUSE) are required. Indeed, the latter have been recently obtained by another team.

4.2.2 Nuclear bar

The presence of an additional nuclear bar has been suggested by NIR imaging (Alonso-Herrero et al. 1998) and by light distribution modelling from *HST* imaging (Läsker et al. 2016). The extension of (SMA) this nuclear bar is ∼2 arcsec, and it is offset from the large-scale bar by 10°−20°.

Considering that both the PA and extension of the inner features of our CO J:2-1 data agree with those of the nuclear bar, we build
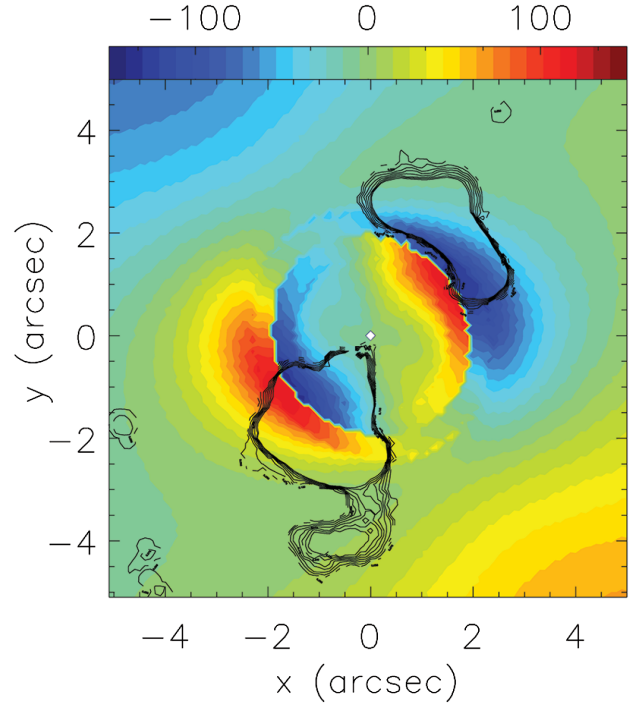

Figure 17. Velocity field of the best-fitting bar perturbation model for the nuclear bar shown in colour following the colour bar above the panel (units of km s^{-1}). Here the fit was made only to the inner region (inside the grey circle in Fig. 10) CO velocity field. The values of the exponential disc, disc PA, and inclination were fixed to the values outlined in Fig. 11. The best-fitting values obtained were $\theta_{obs} = -85°$, $\epsilon = 0.35$, $\lambda = 0.1$, and $\Omega_p = 73$ km s^{-1} kpc^{-1}.

bar perturbation models for the nuclear bar (Fig. 17), assuming that the nuclear bar is decoupled from the large-scale bar and thus has a larger pattern speed. The disc parameters (exponential disc parameters, disc PA and inclination) were kept fixed to the values used above. Typical ranges were assumed for the free parameters: $0.15 < \lambda < 0.4$, $0.1 < \epsilon < 0.8$, $10 < \Omega_p < 200$ km s^{-1} kpc^{-1}. The best-fitted values obtained were $\lambda = 0.1$, $\Omega_p = 73$ km s^{-1} kpc^{-1} and $\epsilon = 0.35$, and $\theta_{obs} = -85°$. The latter value implies that the large-scale and nuclear bars are almost aligned, and that the nuclear bar is completely embedded in the large-scale bar; which is consistent with the results of Alonso-Herrero et al. (1998), where the PA difference between both bars is in the range of $10°−20°$. The resulting model is overlaid on the PV diagram along the minor axis (Fig. 14), where it can be observed that it follows the same gradient of the inner SE feature and the Keplerian-like fall-off, while it is also close to the gradient of the inner NW feature.

Considering that we can reproduce a similar gradient as that observed in the inner SE feature, it is possible that an interaction of the large-scale bar and the nuclear bar exists. If these components present kinematical coupling, they can share a resonance, usually the ILR for the large-scale bar coincides with the CR of the nuclear bar. If this is the case for NGC 3393 it is possible that the molecular gas observed is near the ILR of the large-scale bar where it can accumulate into rings. However, the presence of an inner bar could, in principle, allow the gas to overcome this limit and continue to flow to the central regions (Shlosman et al. 1989).

This simple toy model indicates that it is feasible that a large-scale and nuclear bars interaction can produce a feature similar to the one observed in the inner region of our ALMA data. However,

C. Finlez et al.

the kinematical coupling between both bars and the consequent complex modelling of its effect is beyond the scope of this paper.

4.3 SMBH

Evidence for a secondary SMBH has been presented by Fabbiano et al. ([2011](#)). This BH is located 0″.6 SW from the nucleus (Fig. [4](#)). As it can be seen in the moment 1 maps of the ionized emission lines, there is no clear kinematical component connected to the position of this posited secondary BH. However, the kinematics of the ionized gas are deeply perturbed by the radio jet and thus any kinematical signature of a secondary SMBH can be easily lost.

An alternative explanation to the unusual gradient observed in the SE component of the molecular gas might be linked to this posited secondary SMBH. A pv-diagram along a PA of 50° centred on the feature (Fig. [14](#)) shows a mostly smooth gradient that goes from ~ -100 to $\sim 100\,\mathrm{km\,s^{-1}}$, which could indicate a nuclear disc related to the secondary SMBH. However, the kinematic and morphological centre of the SE feature does not correspond to the posited position of the secondary BH. Alternatively, the inner CO emission (i.e. both the SE and NW inner components) could be centred around the secondary SMBH; although we cannot rule out this case, it would require a very special geometry. Simpler explanations, such as the nuclear bar perturbations are thus favoured by us. The posited secondary SMBH is located in between the nuclear and the SW source, and while there is no clear detection of another source in that position, the presence of another continuum source here cannot be discarded unequivocally. Thus, while we find no evidence supporting the existence of this secondary SMBH, it is important to note that both the observational and interpretive constraints are not strong enough to disprove the presence of the secondary SMBH.

If we assume that the equatorial outflow is axisymmetric (though we have only detected the blueshifted gas in this outflow) then the mass outflow rate for the equatorial outflow can reach $\dot{M} \sim 0.6$ $\mathrm{M_\odot\,yr^{-1}}$. The outflow rates presented here are a lower limit, as we only consider the ionized gas.

To contrast the outflow rates estimated here, we now estimate the inflow rate necessary to feed the SMBH. The bolometric luminosity estimated using the 2–10 keV luminosity is $2.4 \times 10^{44} - 7.6 \times 10^{44}$ $\mathrm{erg\,s^{-1}}$ (Kondratko et al. [2008](#)). Assuming a standard accretion efficiency of 10 per cent the accretion mass rate required is $\dot{M} = 0.04 - 0.1\,\mathrm{M_\odot\,yr^{-1}}$, a factor ~ 8 lower than our estimated outflow rate, which is not unusual in nearby galaxies (Barbosa et al. [2009](#); Müller-Sánchez et al. [2011](#)).

The difference between inflow and outflow rates can indicate that the outflowing gas does not originate from close to the central engine, but is circumnuclear ISM gas that is being pushed away by the radio jet. While we do not find direct evidence of inflows in the ionized gas, if the SE component of the observed CO J:2-1 molecular gas was inflowing with a velocity of $10\,\mathrm{km\,s^{-1}}$ the necessary inflow rate could be achieved. The total CO mass of the SE feature is $M(\mathrm{H_2}) = 5.4 \times 10^7\,\mathrm{M_\odot}$, assuming $\alpha_{CO} = 4.6\,\mathrm{M_\odot}$ $(\mathrm{K\,km\,s^{-1}\,pc^2})^{-1}$. If all the molecular mass enclosed in the SE feature was inflowing with a velocity of $10\,\mathrm{km\,s^{-1}}$, the potential accretion rate produced would be $0.32\,\mathrm{M_\odot\,yr^{-1}}$. While we do not find direct evidence that the molecular gas is inflowing, a velocity of $10\,\mathrm{km\,s^{-1}}$ would fall under the detection limit of our analysis, and the interaction between the large scale and nuclear bar can make this inflow possible.

5 CONCLUSIONS

We have analysed the kinematics of the stars, ionized gas, and molecular gas in the central kpcs of the Seyfert 2 galaxy NGC 3393 using optical integral field observations from GEMINI–GMOS/IFU and ALMA. From our detailed analysis of these data we conclude that

(1) NGC 3393 presents a complex multiphase ISM, with strong interactions between the nuclear radio jet and the ionized gas produces complex kinematics. We have found that it is necessary to fit the emission line profiles observed with multiple Gaussian components. We identify three components in the ionized gas, which we refer to as the narrow, broad redshifted, and broad blueshifted components.

(2) The narrow ionized gas component has a low velocity dispersion ($\sigma < 115\,\mathrm{km\,s^{-1}}$) and, more or less, follows pure rotation in the galaxy disc; nevertheless this component is perturbed in the regions near the radio lobes.

(3) The broad redshifted component ($115 < \sigma < 230\,\mathrm{km\,s^{-1}}$) can be observed in regions near the radio lobes. We identify two outflows in this component named as 'O2' and 'O3'. 'O2' seems associated to the NE radio lobe, while 'O3' is near the SW radio lobe. The 'O2' outflow is redshifted on the far side of the galaxy which can indicate gas being pushed away by the radio jet. As the SW radio lobe appears to be the approaching component of the radio jet, it is possible that this jet is starting to leave the galaxy in the region of the 'O3' outflow, and thus the redshifted gas observed can be gas in the disc, being pushed away from the line of sight by the radio jet, or if the jet remains in the disc the outflow is produced by the gas being pushed by the jet inside the disc plane.

(4) The broad blueshifted component ($115 < \sigma < 230\,\mathrm{km\,s^{-1}}$) presents large blueshifted velocities distributed along the equatorial region, perpendicular to the radio jet axis. A weaker redshifted wing is also visible in the same region. We interpret this component as being part of an equatorial outflow, expanding perpendicular to the radio jet axis, and whose emission is attenuated by dust in the plane of the galaxy.

(5) From the measured velocities, $\mathrm{H}\alpha$ fluxes, and electron densities, of the outflowing components, we estimate a total outflow rate of $\dot{M} \sim 0.13\,\mathrm{M_\odot\,yr^{-1}}$ for the jet-driven outflows, and $\dot{M} \sim 0.24$ $\mathrm{M_\odot\,yr^{-1}}$ for the equatorial outflow. If we consider a symmetric component for the equatorial outflow, the total outflow rate can reach $\dot{M} \sim 0.6\,\mathrm{M_\odot\,yr^{-1}}$ for the ionized gas. This outflow rate is ~ 8 times larger than the accretion rate necessary to fuel the AGN. While we found no direct evidence for gas inflows, we note that the necessary inflow rate can be provided if the SE component of the CO J:2-1 emission is inflowing at a velocity of $\sim 10\,\mathrm{km\,s^{-1}}$, a velocity which would be close to the detection limit of our observations and analysis.

(6) We were forced to analyse the kinematics for the CO J:2-1 emission separately for two regions, an inner region within 5 arcsec of the nucleus, and the region outside said circle, since we could not find a global model that could fit both regions together. We do not detect CO J:2-1 emission at either position of the SMBH or at the position of the posited secondary SMBH.

(7) The outer region of the CO J:2-1 emission seems to trace the rotation in the outer disc, and can be fitted with an exponential disc rotation model, though obvious residuals remain. To understand the role of the large-scale bar in the kinematics observed on the CO J:2-1 emission we applied the harmonic decomposition formalism to the CO velocity field. Specifically, we fitted a bar-perturbation model to the outer region of our CO J:2-1 velocity field. We found,

MNRAS **479**, 3892–3908 (2018)

Downloaded from https://academic.oup.com/mnras/article-abstract/479/3/3892/5037937 by Universidade Federal do Rio Grande do Sul user on 07 November 2018

over a range of different Ω_p and λ, the presence of a resonance between the inner and outer region, and a resonance that encloses the outer region of the CO emission. These resonances could explain the difference in PA found in the ALMA and GEMINI–GMOS/IFU data compared to the large-scale kinematics observed by Cooke et al. (2000), and the observed distribution of CO J:2-1 emission. This model, however, does not fit the observed CO kinematics of the inner region.

(8) The inner region of the CO J:2-1 emission presents highly disturbed kinematics, with the presence of an off-nuclear velocity gradient centred in the SE component. We found this gradient cannot be explained by the large-scale bar model, nor by the presence of the posited secondary SMBH or any disc related to it. We fitted a second bar perturbation model based on the parameters of the nuclear bar and found a good fit to the inner region kinematics. This toy model indicates that the kinematics observed in the inner region of the CO J:2-1 emission can be attributed solely, or at least dominantly, to perturbation by the nuclear bar, together with interactions between the large-scale and nuclear bars.

ACKNOWLEDGEMENTS

REFERENCES

Allington-Smith J. et al., 2002, PASP, 114, 892
Alonso-Herrero A., Simpson C., Ward M. J., Wilson A. S., 1998, ApJ, 495, 196
Antonuccio-Delogu V., Silk J., 2010, MNRAS, 405, 1303
Athanassoula E., 1992, MNRAS, 259, 345
Barbosa F. K. B., Storchi-Bergmann T., Cid Fernandes R., Winge C., Schmitt H., 2009, MNRAS, 396, 2
Bertola F., Bettoni D., Danziger J., Sadler E., Sparke L., de Zeeuw T., 1991, ApJ, 373, 369
Best P. N., Carilli C. L., Garrington S. T., Longair M. S., Rottgering H. J. A., 1998, MNRAS, 299, 357
Best P. N., Kauffmann G., Heckman T. M., Ivezić Ž., 2005, MNRAS, 362, 9
Bianchi S., Guainazzi M., Chiaberge M., 2006, A&A, 448, 499
Cappellari M., 2017, MNRAS, 466, 798
Cappellari M., Copin Y., 2003, MNRAS, 342, 345
Cappellari M., Emsellem E., 2004, PASP, 116, 138
Cheung E. et al., 2015, MNRAS, 447, 506
Cisternas M. et al., 2013, ApJ, 776, 50
Combes F., 2001, in Aretxaga I., Kunth D., Mujica R., eds, Proceedings of a conference held in Tonantzintla, Puebla, Mexico, 26-30 June, 2000: Advanced Lectures on the Starburst-AGN. World Scientific, Singapore, p. 223
Combes F., Gerin M., 1985, A&A, 150, 327
Cooke A. J., Baldwin J. A., Ferland G. J., Netzer H., Wilson A. S., 2000, ApJS, 129, 517
Couto G. S., Storchi-Bergmann T., Schnorr-Müller A., 2017, MNRAS, 469, 1573
Croton D. J. et al., 2006, MNRAS, 365, 11
Das V., Crenshaw D. M., Kraemer S. B., 2007, ApJ, 656, 699
Dasyra K. M., Combes F., 2012, A&A, 541, L7
de Vaucouleurs G., de Vaucouleurs A., Corwin H. G., Jr, Buta R. J., Paturel G., Fouqué P., 1991, Third Reference Catalogue of Bright Galaxies. Volume I: Explanations and references. Volume II: Data for galaxies between 0^h and 12^h. Volume III: Data for galaxies between 12^h and 24^h. Springer-Verlag, New York
Di Matteo T., Springel V., Hernquist L., 2005, Nature, 433, 604
Dumas G., Mundell C. G., Emsellem E., Nagar N. M., 2007, MNRAS, 379, 1249
Elitzur M., 2012, ApJ, 747, L33
Emsellem E., Greusard D., Friedli D., Combes F., 2001a, in Funes J. G., Corsini E. M., eds, ASP Conf. Ser., Vol. 230, Galaxy Disks and Disk Galaxies. Astron. Soc. Pac., San Francisco, p. 235
Emsellem E., Greusard D., Combes F., Friedli D., Leon S., Pécontal E., Wozniak H., 2001b, A&A, 368, 52
Fabbiano G., Wang J., Elvis M., Risaliti G., 2011, Nature, 477, 431
Fabian A. C., 2012, ARA&A, 50, 455
Fan L. et al., 2016, ApJ, 822, L32
Ferrarese L., Ford H., 2005, Space Sci. Rev., 116, 523
Ferrarese L., Merritt D., 2000, ApJ, 539, L9
Fischer T. C., Crenshaw D. M., Kraemer S. B., Schmitt H. R., 2013, ApJS, 209, 1
Franx M., van Gorkom J. H., de Zeeuw T., 1994, ApJ, 436, 642
Galloway M. A. et al., 2015, MNRAS, 448, 3442
García-Burillo S., Combes F., Schinnerer E., Boone F., Hunt L. K., 2005, A&A, 441, 1011
Gebhardt K. et al., 2000, ApJ, 539, L13
Goulding A. D. et al., 2017, ApJ, 843, 135
Goulding A. D. et al., 2018, PASJ, 70, 37
Hardcastle M. J. et al., 2013, MNRAS, 429, 2407
Ho L. C., Filippenko A. V., Sargent W. L. W., 1997, ApJS, 112, 315
Holt J., Tadhunter C. N., Morganti R., Emonts B. H. C., 2011, MNRAS, 410, 1527
Hönig S. F. et al., 2013, ApJ, 771, 87
Hook I. M., Jørgensen I., Allington-Smith J. R., Davies R. L., Metcalfe N., Murowinski R. G., Crampton D., 2004, PASP, 116, 425
Hopkins P. F., Kocevski D. D., Bundy K., 2014, MNRAS, 445, 823
Jarvis M. J. et al., 2001, MNRAS, 326, 1563
Jungwiert B., Combes F., Axon D. J., 1997, A&AS, 125
Kay L. E., Tran H. D., Magalhães A. M., 2002, Bull. Am. Astron. Soc., 34, 646
Kewley L. J., Groves B., Kauffmann G., Heckman T., 2006, MNRAS, 372, 961
Kim W.-T., Seo W.-Y., Stone J. M., Yoon D., Teuben P. J., 2012, ApJ, 747, 60
Knapen J. H., Shlosman I., Peletier R. F., 2000, ApJ, 529, 93
Kondratko P. T., Greenhill L. J., Moran J. M., 2008, ApJ, 678, 87
Kormendy J., Ho L. C., 2013, ARA&A, 51, 511
Kormendy J., Richstone D., 1995, ARA&A, 33, 581
Koss M. J. et al., 2015, ApJ, 807, 149
Läsker R., Greene J. E., Seth A., van de Ven G., Braatz J. A., Henkel C., Lo K. Y., 2016, ApJ, 825, 3
Lena D., 2014, preprint (arXiv:1409.8264)
Lena D. et al., 2015a, ApJ, 806, 84
Lena D. et al., 2015b, ApJ, 806, 84
Lena D., Robinson A., Storchi-Bergmann T., Couto G. S., Schnorr-Müller A., Riffel R. A., 2016, MNRAS, 459, 4485
Levenson N. A., Heckman T. M., Krolik J. H., Weaver K. A., Życki P. T., 2006, ApJ, 648, 111
Li J., Ostriker J., Sunyaev R., 2013, ApJ, 767, 105
Lin C. C., Shu F. H., 1964, ApJ, 140, 646

Lindblad B., 1964, Astrophys. Nor., 9, 103

Lindblad P. O., Lindblad P. A. B., 1994, in King I. R., ed., ASP Conf. Ser. Vol. 66, Physics of the Gaseous and Stellar Disks of the Galaxy. Astron. Soc. Pac., San Francisco, p. 29

Lindblad P. A. B., Lindblad P. O., Athanassoula E., 1996, A&A, 313, 65

Liu G., Zakamska N. L., Greene J. E., Nesvadba N. P. H., Liu X., 2013, MNRAS, 436, 2576

Maksym W. P., Fabbiano G., Elvis M., Karovska M., Paggi A., Raymond J., Wang J., Storchi-Bergmann T., 2017, ApJ, 844, 69

Markwardt C. B., 2009, in Bohlender D. A., Durand D., Dowler P., eds, ASP Conf. Ser. Vol. 411, Astronomical Data Analysis Software and Systems XVIII. Astron. Soc. Pac., San Francisco, p. 251

Martini P., Pogge R. W., 1999, AJ, 118, 2646

Martini P., Dicken D., Storchi-Bergmann T., 2013, ApJ, 766, 121

Meyer M. J. et al., 2004, MNRAS, 350, 1195

Morganti R., Oosterloo T. A., Tadhunter C. N., van Moorsel G., Emonts B., 2005, A&A, 439, 521

Müller-Sánchez F., Prieto M. A., Hicks E. K. S., Vives-Arias H., Davies R. I., Malkan M., Tacconi L. J., Genzel R., 2011, ApJ, 739, 69

Mundell C. G., Shone D. L., 1999, MNRAS, 304, 475

Nesvadba N. P. H., Lehnert M. D., Eisenhauer F., Gilbert A., Tecza M., Abuter R., 2006, ApJ, 650, 693

Osterbrock D. E., 1989, Astrophysics of Gaseous Nebulae and Active Galactic Nuclei. University Science Books, Mill Valley, CA, p. 422

Paturel G., Theureau G., Bottinelli L., Gouguenheim L., Coudreau-Durand N., Hallet N., Petit C., 2003, A&A, 412, 57

Pogge R. W., 1997, in Peterson B. M., Cheng F.-Z., Wilson A. S., eds, ASP Conf. Ser. Vol. 113, IAU Colloq. 159: Emission Lines in Active Galaxies: New Methods and Techniques. Astron. Soc. Pac., San Francisco, p. 378

Ramos Almeida C., Martínez González M. J., Asensio Ramos A., Acosta-Pulido J. A., Hönig S. F., Alonso-Herrero A., Tadhunter C. N., González-Martín O., 2016, MNRAS, 461, 1387

Riffel R. A., 2010, Ap&SS, 327, 239

Riffel R. A., Storchi-Bergmann T., Winge C., Barbosa F. K. B., 2006, MNRAS, 373, 2

Riffel R. A., Storchi-Bergmann T., Riffel R., 2014, ApJ, 780, L24

Riffel R. A., Storchi-Bergmann T., Riffel R., 2015, MNRAS, 451, 3587

Schmitt H. R., Kinney A. L., 1996, ApJ, 463, 498

Schmitt H. R., Antonucci R. R. J., Ulvestad J. S., Kinney A. L., Clarke C. J., Pringle J. E., 2001, ApJ, 555, 663

Schmitt H. R., Donley J. L., Antonucci R. R. J., Hutchings J. B., Kinney A. L., 2003, ApJS, 148, 327

Schnorr-Müller A., Storchi-Bergmann T., Robinson A., Lena D., Nagar N. M., 2016, MNRAS, 457, 972

Schnorr-Müller A., Storchi-Bergmann T., Nagar N. M., Robinson A., Lena D., 2017, MNRAS, 471, 3888

Schoenmakers R. H. M., Franx M., de Zeeuw P. T., 1997a, MNRAS, 292, 349

Schoenmakers R. H. M., Franx M., de Zeeuw P. T., 1997b, MNRAS, 292, 349

Sellwood J. A., 1981, A&A, 99, 362

Shlosman I., Frank J., Begelman M. C., 1989, Nature, 338, 45

Silk J., Nusser A., 2010, ApJ, 725, 556

Simões Lopes R. D., Storchi-Bergmann T., de Fatima Saraiva M., Martini P., 2007, ApJ, 655, 718

Storchi-Bergmann T., Dors Jr. O. L., Riffel R. A., Fathi K., Axon D. J., Robinson A., Marconi A., Ostlin G., 2007, ApJ, 670, 959

Storchi-Bergmann T., Lopes R. D. S., McGregor P. J., Riffel R. A., Beck T., Martini P., 2010, MNRAS, 402, 819

Treister E., Schawinski K., Urry C. M., Simmons B. D., 2012, ApJ, 758, L39

Valdes F., Gupta R., Rose J. A., Singh H. P., Bell D. J., 2004, ApJS, 152, 251

Véron-Cetty M.-P., Véron P., 2003, A&A, 412, 399

Wada K., 1994, PASJ, 46, 165

Wagner A. Y., Bicknell G. V., 2011, ApJ, 728, 29

Wagner A. Y., Bicknell G. V., Umemura M., 2012, ApJ, 757, 136

Whittle M., 1985, MNRAS, 213, 1

Wong T., Blitz L., Bosma A., 2004, ApJ, 605, 183

This paper has been typeset from a TEX/LATEX file prepared by the author.